

Elastic J/ψ Production at HERA

H1 Collaboration

Abstract

Cross sections for elastic production of J/ψ mesons in photoproduction and electroproduction are measured in electron proton collisions at HERA using an integrated luminosity of 55 pb^{-1} . Results are presented for photon virtualities Q^2 up to 80 GeV^2 . The dependence on the photon-proton centre of mass energy $W_{\gamma p}$ is analysed in the range $40 \leq W_{\gamma p} \leq 305 \text{ GeV}$ in photoproduction and $40 \leq W_{\gamma p} \leq 160 \text{ GeV}$ in electroproduction. The $W_{\gamma p}$ dependences of the cross sections do not change significantly with Q^2 and can be described by models based on perturbative QCD. Within such models, the data show a high sensitivity to the gluon density of the proton in the domain of low Bjorken x and low Q^2 . Differential cross sections $d\sigma/dt$, where t is the squared four-momentum transfer at the proton vertex, are measured in the range $|t| < 1.2 \text{ GeV}^2$ as functions of $W_{\gamma p}$ and Q^2 . Effective Pomeron trajectories are determined for photoproduction and electroproduction. The J/ψ production and decay angular distributions are consistent with s -channel helicity conservation. The ratio of the cross sections for longitudinally and transversely polarised photons is measured as a function of Q^2 and is found to be described by perturbative QCD based models.

Submitted to *Eur. Phys. J. C*

A. Aktas¹⁰, V. Andreev²⁶, T. Anthonis⁴, B. Antunovic²⁷, S. Aplin¹⁰, A. Asmone³⁴,
 A. Astvatsatourov⁴, A. Babaev²⁵, S. Backovic³¹, J. Bähr³⁹, A. Baghdasaryan³⁸, P. Baranov²⁶,
 E. Barrelet³⁰, W. Bartel¹⁰, S. Baudrand²⁸, S. Baumgartner⁴⁰, J. Becker⁴¹, M. Beckingham¹⁰,
 O. Behnke¹³, O. Behrendt⁷, A. Belousov²⁶, Ch. Berger¹, N. Berger⁴⁰, J.C. Bizot²⁸,
 M.-O. Boenig⁷, V. Boudry²⁹, J. Bracinik²⁷, G. Brandt¹³, V. Brisson²⁸, D. Bruncko¹⁶,
 F.W. Büsser¹¹, A. Bunyatyan^{12,38}, G. Buschhorn²⁷, L. Bystritskaya²⁵, A.J. Campbell¹⁰,
 S. Caron¹, F. Cassol-Brunner²², K. Cerny³³, V. Cerny^{16,47}, V. Chekelian²⁷, J.G. Contreras²³,
 J.A. Coughlan⁵, B.E. Cox²¹, G. Cozzika⁹, J. Cvach³², J.B. Dainton¹⁸, W.D. Dau¹⁵,
 K. Daum^{37,43}, Y. de Boer²⁵, B. Delcourt²⁸, M. Del Degan⁴⁰, A. De Roeck^{10,45}, K. Desch¹¹,
 E.A. De Wolf⁴, C. Diaconu²², V. Dodonov¹², A. Dubak^{31,46}, G. Eckerlin¹⁰, V. Efremenko²⁵,
 S. Egli³⁶, R. Eichler³⁶, F. Eisele¹³, M. Ellerbrock¹³, E. Elsen¹⁰, W. Erdmann⁴⁰, S. Essenov²⁵,
 A. Falkewicz⁶, P.J.W. Faulkner³, L. Favart⁴, A. Fedotov²⁵, R. Felst¹⁰, J. Ferencei¹⁶, L. Finke¹¹,
 M. Fleischer¹⁰, P. Fleischmann¹⁰, G. Flucke¹⁰, A. Fomenko²⁶, I. Foresti⁴¹, G. Franke¹⁰,
 T. Frisson²⁹, E. Gabathuler¹⁸, E. Garutti¹⁰, J. Gayler¹⁰, C. Gerlich¹³, S. Ghazaryan³⁸,
 S. Ginzburgskaya²⁵, A. Glazov¹⁰, I. Glushkov³⁹, L. Goerlich⁶, M. Goettlich¹⁰, N. Gogitidze²⁶,
 S. Gorbounov³⁹, C. Goyon²², C. Grab⁴⁰, T. Greenshaw¹⁸, M. Gregori¹⁹, B.R. Grell¹⁰,
 G. Grindhammer²⁷, C. Gwilliam²¹, D. Haidt¹⁰, L. Hajduk⁶, M. Hansson²⁰, G. Heinzelmann¹¹,
 R.C.W. Henderson¹⁷, H. Henschel³⁹, O. Henshaw³, G. Herrera²⁴, M. Hildebrandt³⁶,
 K.H. Hiller³⁹, D. Hoffmann²², R. Horisberger³⁶, A. Hovhannisyan³⁸, T. Hreus¹⁶, S. Hussain¹⁹,
 M. Ibbotson²¹, M. Ismail²¹, M. Jacquet²⁸, L. Janauschek²⁷, X. Janssen¹⁰, V. Jemanov¹¹,
 L. Jönsson²⁰, D.P. Johnson⁴, A.W. Jung¹⁴, H. Jung^{20,10}, M. Kapichine⁸, J. Katzy¹⁰,
 I.R. Kenyon³, C. Kiesling²⁷, M. Klein³⁹, C. Kleinwort¹⁰, T. Klimkovich¹⁰, T. Kluge¹⁰,
 G. Knies¹⁰, A. Knutsson²⁰, V. Korbel¹⁰, P. Kostka³⁹, K. Krastev¹⁰, J. Kretzschmar³⁹,
 A. Kropivnitskaya²⁵, K. Krüger¹⁴, J. Kückens¹⁰, M.P.J. Landon¹⁹, W. Lange³⁹,
 T. Laštovička^{39,33}, G. Laštovička-Medin³¹, P. Laycock¹⁸, A. Lebedev²⁶, G. Leibenguth⁴⁰,
 V. Lendermann¹⁴, S. Levonian¹⁰, L. Lindfeld⁴¹, K. Lipka³⁹, A. Liptaj²⁷, B. List⁴⁰, J. List¹¹,
 E. Lobodzinska^{39,6}, N. Loktionova²⁶, R. Lopez-Fernandez¹⁰, V. Lubimov²⁵,
 A.-I. Lucaci-Timoce¹⁰, H. Lueders¹¹, D. Lüke^{7,10}, T. Lux¹¹, L. Lytkin¹², A. Makankine⁸,
 N. Malden²¹, E. Malinovski²⁶, S. Mangano⁴⁰, P. Marage⁴, R. Marshall²¹, M. Martisikova¹⁰,
 H.-U. Martyn¹, S.J. Maxfield¹⁸, D. Meer⁴⁰, A. Mehta¹⁸, K. Meier¹⁴, A.B. Meyer¹¹,
 H. Meyer³⁷, J. Meyer¹⁰, S. Mikocki⁶, I. Milcewicz-Mika⁶, D. Milstead¹⁸, D. Mladenov³⁵,
 A. Mohamed¹⁸, F. Moreau²⁹, A. Morozov⁸, J.V. Morris⁵, M.U. Mozer¹³, K. Müller⁴¹,
 P. Murín^{16,44}, K. Nankov³⁵, B. Naroska¹¹, Th. Naumann³⁹, P.R. Newman³, C. Niebuhr¹⁰,
 A. Nikiforov²⁷, D. Nikitin⁸, G. Nowak⁶, M. Nozicka³³, R. Oganezov³⁸, B. Olivier³,
 J.E. Olsson¹⁰, S. Osman²⁰, D. Ozerov²⁵, V. Palichik⁸, I. Panagoulas¹⁰, T. Papadopoulou¹⁰,
 C. Pascaud²⁸, G.D. Patel¹⁸, M. Peez²⁹, E. Perez⁹, D. Perez-Astudillo²³, A. Perieanu¹⁰,
 A. Petrukhin²⁵, D. Pitzl¹⁰, R. Plačákytė²⁷, B. Portheault²⁸, B. Povh¹², P. Prideaux¹⁸,
 A.J. Rahmat¹⁸, N. Raicevic³¹, P. Reimer³², A. Rimmer¹⁸, C. Risler¹⁰, E. Rizvi¹⁹,
 P. Robmann⁴¹, B. Roland⁴, R. Roosen⁴, A. Rostovtsev²⁵, Z. Rurikova²⁷, S. Rusakov²⁶,
 F. Salvaire¹¹, D.P.C. Sankey⁵, E. Sauvan²², S. Schätzel¹⁰, F.-P. Schilling¹⁰, D. Schmidt¹⁰,
 S. Schmidt¹⁰, S. Schmitt¹⁰, C. Schmitz⁴¹, L. Schoeffel⁹, A. Schöning⁴⁰,
 H.-C. Schultz-Coulon¹⁴, K. Sedlák³², F. Sefkow¹⁰, R.N. Shaw-West³, I. Sheviakov²⁶,
 L.N. Shtarkov²⁶, T. Sloan¹⁷, P. Smirnov²⁶, Y. Soloviev²⁶, D. South¹⁰, V. Spaskov⁸,
 A. Specka²⁹, B. Stella³⁴, J. Stiewe¹⁴, I. Strauch¹⁰, U. Straumann⁴¹, V. Tchoulakov⁸,
 G. Thompson¹⁹, P.D. Thompson³, F. Tomasz¹⁶, D. Traynor¹⁹, P. Truöl⁴¹, I. Tsakov³⁵,
 G. Tsipolitis^{10,42}, I. Tsurin¹⁰, J. Turnau⁶, E. Tzamariudaki²⁷, M. Urban⁴¹, A. Usik²⁶,

D. Utkin²⁵, A. Valkárová³³, C. Vallée²², P. Van Mechelen⁴, A. Vargas Trevino⁷, Y. Vazdik²⁶, C. Veelken¹⁸, A. Vest¹, S. Vinokurova¹⁰, V. Volchinski³⁸, K. Wacker⁷, J. Wagner¹⁰, G. Weber¹¹, R. Weber⁴⁰, D. Wegener⁷, C. Werner¹³, M. Wessels¹⁰, B. Wessling¹⁰, C. Wigmore³, Ch. Wissing⁷, R. Wolf¹³, E. Wünsch¹⁰, S. Xella⁴¹, W. Yan¹⁰, V. Yeganov³⁸, J. Žáček³³, J. Zálešák³², Z. Zhang²⁸, A. Zhelezov²⁵, A. Zhokin²⁵, Y.C. Zhu¹⁰, J. Zimmermann²⁷, T. Zimmermann⁴⁰, H. Zohrabyan³⁸, and F. Zomer²⁸

¹ *I. Physikalisches Institut der RWTH, Aachen, Germany^a*

² *III. Physikalisches Institut der RWTH, Aachen, Germany^a*

³ *School of Physics and Astronomy, University of Birmingham, Birmingham, UK^b*

⁴ *Inter-University Institute for High Energies ULB-VUB, Brussels; Universiteit Antwerpen, Antwerpen; Belgium^c*

⁵ *Rutherford Appleton Laboratory, Chilton, Didcot, UK^b*

⁶ *Institute for Nuclear Physics, Cracow, Poland^d*

⁷ *Institut für Physik, Universität Dortmund, Dortmund, Germany^a*

⁸ *Joint Institute for Nuclear Research, Dubna, Russia*

⁹ *CEA, DSM/DAPNIA, CE-Saclay, Gif-sur-Yvette, France*

¹⁰ *DESY, Hamburg, Germany*

¹¹ *Institut für Experimentalphysik, Universität Hamburg, Hamburg, Germany^a*

¹² *Max-Planck-Institut für Kernphysik, Heidelberg, Germany*

¹³ *Physikalisches Institut, Universität Heidelberg, Heidelberg, Germany^a*

¹⁴ *Kirchhoff-Institut für Physik, Universität Heidelberg, Heidelberg, Germany^a*

¹⁵ *Institut für Experimentelle und Angewandte Physik, Universität Kiel, Kiel, Germany*

¹⁶ *Institute of Experimental Physics, Slovak Academy of Sciences, Košice, Slovak Republic^f*

¹⁷ *Department of Physics, University of Lancaster, Lancaster, UK^b*

¹⁸ *Department of Physics, University of Liverpool, Liverpool, UK^b*

¹⁹ *Queen Mary and Westfield College, London, UK^b*

²⁰ *Physics Department, University of Lund, Lund, Sweden^g*

²¹ *Physics Department, University of Manchester, Manchester, UK^b*

²² *CPPM, CNRS/IN2P3 - Univ. Mediterranee, Marseille - France*

²³ *Departamento de Fisica Aplicada, CINVESTAV, Mérida, Yucatán, México^k*

²⁴ *Departamento de Fisica, CINVESTAV, México^k*

²⁵ *Institute for Theoretical and Experimental Physics, Moscow, Russia^l*

²⁶ *Lebedev Physical Institute, Moscow, Russia^e*

²⁷ *Max-Planck-Institut für Physik, München, Germany*

²⁸ *LAL, Université de Paris-Sud, IN2P3-CNRS, Orsay, France*

²⁹ *LLR, Ecole Polytechnique, IN2P3-CNRS, Palaiseau, France*

³⁰ *LPNHE, Universités Paris VI and VII, IN2P3-CNRS, Paris, France*

³¹ *Faculty of Science, University of Montenegro, Podgorica, Serbia and Montenegro^e*

³² *Institute of Physics, Academy of Sciences of the Czech Republic, Praha, Czech Republic^{e,i}*

³³ *Faculty of Mathematics and Physics, Charles University, Praha, Czech Republic^{e,i}*

³⁴ *Dipartimento di Fisica Università di Roma Tre and INFN Roma 3, Roma, Italy*

³⁵ *Institute for Nuclear Research and Nuclear Energy, Sofia, Bulgaria^e*

³⁶ *Paul Scherrer Institut, Villigen, Switzerland*

³⁷ *Fachbereich C, Universität Wuppertal, Wuppertal, Germany*

³⁸ *Yerevan Physics Institute, Yerevan, Armenia*

³⁹ DESY, Zeuthen, Germany

⁴⁰ Institut für Teilchenphysik, ETH, Zürich, Switzerland^j

⁴¹ Physik-Institut der Universität Zürich, Zürich, Switzerland^j

⁴² Also at Physics Department, National Technical University, Zografou Campus, GR-15773 Athens, Greece

⁴³ Also at Rechenzentrum, Universität Wuppertal, Wuppertal, Germany

⁴⁴ Also at University of P.J. Šafárik, Košice, Slovak Republic

⁴⁵ Also at CERN, Geneva, Switzerland

⁴⁶ Also at Max-Planck-Institut für Physik, München, Germany

⁴⁷ Also at Comenius University, Bratislava, Slovak Republic

^a Supported by the Bundesministerium für Bildung und Forschung, FRG, under contract numbers 05 H1 1GUA /1, 05 H1 1PAA /1, 05 H1 1PAB /9, 05 H1 1PEA /6, 05 H1 1VHA /7 and 05 H1 1VHB /5

^b Supported by the UK Particle Physics and Astronomy Research Council, and formerly by the UK Science and Engineering Research Council

^c Supported by FNRS-FWO-Vlaanderen, IISN-IKW and IWT and by Interuniversity Attraction Poles Programme, Belgian Science Policy

^d Partially Supported by the Polish State Committee for Scientific Research, SPUB/DESY/P003/DZ 118/2003/2005

^e Supported by the Deutsche Forschungsgemeinschaft

^f Supported by VEGA SR grant no. 2/4067/ 24

^g Supported by the Swedish Natural Science Research Council

ⁱ Supported by the Ministry of Education of the Czech Republic under the projects LC527 and INGO-IP05LA259

^j Supported by the Swiss National Science Foundation

^k Supported by CONACYT, México, grant 400073-F

^l Partly Supported by Russian Foundation for Basic Research, grants 03-02-17291 and 04-02-16445

1 Introduction

Quantum Chromodynamics (QCD), the field theory of quark and gluon interactions, is expected to describe the strong force between hadrons. QCD is a successful theory in the limit of short distances, corresponding to small values of the strong coupling constant α_s , where perturbative methods can be applied (perturbative QCD, pQCD). The bulk of the scattering cross section of hadrons however, is dominated by long-range forces (“soft interactions”), where a satisfactory understanding of QCD still remains a challenge. A large fraction of these soft interactions is mediated by vacuum quantum number exchange and is termed “diffractive”. In hadronic interactions, diffraction is well described by Regge theory, where it is due to the t -channel exchange of a leading trajectory with vacuum quantum numbers, called the “Pomeron” trajectory. In the high energy limit, Pomeron exchange dominates over all other contributions to the scattering amplitude and leads to an almost energy-independent total cross section. Elastic photoproduction of vector mesons, $\gamma p \rightarrow VM p$, is a particular example for a diffractive process. Measurements of the cross sections for the elastic production of light vector mesons (ρ , ω , and ϕ) in low Q^2 electron-proton collisions at HERA as function of the photon-proton centre of mass energy $W_{\gamma p}$ [1, 2] have verified the expected universal Regge behaviour.

The cross section for elastic photoproduction of J/ψ mesons, $\gamma p \rightarrow J/\psi p$, on the contrary, rises steeply with $W_{\gamma p}$ [3–6], incompatible with a universal Pomeron. Due to the large mass of the J/ψ meson, which provides a “hard” scale (equivalent to a short range of the forces involved), the elastic photoproduction of J/ψ mesons is expected to be described by pQCD. In electroproduction the photon virtuality Q^2 can provide a second hard scale in addition to the J/ψ mass, allowing the interplay between these two scales to be studied.

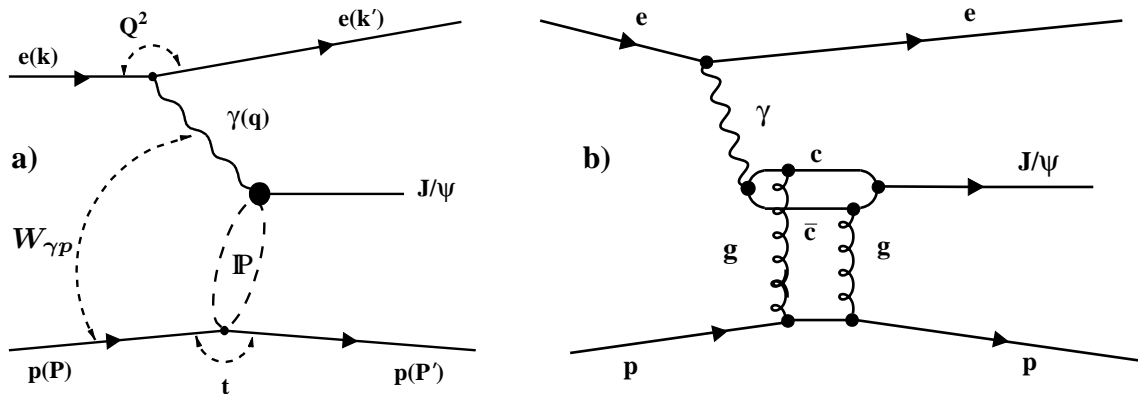


Figure 1: Elastic J/ψ production, a) in an approach based on Pomeron (\mathbb{P}) exchange and b) in a pQCD approach via two gluon exchange. The kinematic variables are indicated in a).

The elastic production of J/ψ mesons is illustrated in figure 1. In QCD at lowest order the process is mediated by a colour-singlet state of two gluons (figure 1b) and the cross section is related to the square of the gluon density in the proton. The gluon’s momentum fraction x is kinematically related to $W_{\gamma p}$: the steep rise in the gluon density towards low values of x thus explains the steep rise of the cross section with increasing $W_{\gamma p}$ observed in the data. Beyond this approximation correlations between the gluons have to be taken into account and the cross

section for elastic J/ψ production involves the generalised gluon density (see for example [7] for a review).

The dependence of the elastic J/ψ cross sections on the squared four-momentum transfer t at the proton vertex shows a fast fall with increasing $|t|$. This dependence can be parameterised as an exponential function e^{bt} at low values of $|t|$, although other shapes have also been proposed (for example [8]). In Regge theory with a t dependent Pomeron trajectory, the t dependence of the cross section varies with $W_{\gamma p}$, the slope parameter b increasing logarithmically with $W_{\gamma p}$ (“shrinkage” of the diffractive peak). In QCD-based models, on the other hand, the dependence of b on $W_{\gamma p}$ is expected to be weak [9, 10]. In addition to the elastic process, in which the proton remains intact, diffractive J/ψ production can lead to proton dissociation, $\gamma p \rightarrow J/\psi Y$, in which a low mass baryonic state Y is produced. This process is expected to be important at large values of $|t|$.

In the past, diffractive J/ψ cross sections have been measured using photon and electron beams in fixed target experiments up to centre of mass energies of about 20 GeV. At HERA the kinematic range is extended up to photon-proton centre of mass energies of $W_{\gamma p} \sim 290$ GeV in photoproduction, and in electroproduction up to photon virtualities of $Q^2 \lesssim 100$ GeV² [1, 3–6, 11–16]. In this paper new data are presented on the Q^2 , $W_{\gamma p}$ and t dependence of the cross section for elastic J/ψ production. The data correspond to a factor of three more integrated luminosity than our previous publication for photoproduction [4] and a factor of two more for electroproduction [11]. The kinematic range is extended to values of $W_{\gamma p}$ up to 305 GeV in photoproduction, while in electroproduction the range covered is $40 < W_{\gamma p} < 160$ GeV. Furthermore, the angular distributions for production and decay of the J/ψ mesons are determined in order to extract the cross sections of longitudinally and transversely polarised photons and to test the hypothesis of s -channel helicity conservation (SCHC), which predicts that the helicity of the J/ψ meson in the final state is the same as that of the initial (virtual) photon.

2 Models for Elastic J/ψ Production

Within the Regge framework (see for example [17] for a review) the cross section for diffractive photoproduction of vector mesons at low values of $|t|$ approximately follows a power law $\sigma_{\gamma p} \propto W_{\gamma p}^\delta$ with $\delta \simeq 0.2$ [18]. The power is related to the Pomeron trajectory $\delta \sim 4(\alpha_{IP}(t) - 1)$ where $\alpha_{IP}(t) = \alpha_{IP}(0) + \alpha'_{IP}t$. The existing measurements for J/ψ mesons, however, indicate a much steeper dependence on $W_{\gamma p}$ ($\delta \simeq 0.8$) than is predicted by the universal (“soft”) Pomeron. There are also indications that the slope α'_{IP} , responsible for the shrinkage of the diffractive peak of elastic J/ψ photoproduction, is smaller [4] than the value of 0.25 GeV⁻² expected from the soft Pomeron trajectory. To overcome this difficulty, Donnachie and Landshoff have suggested an additional “hard” Pomeron trajectory [19] for processes which involve a hard scale, such as the vector meson mass or a large momentum transfer Q^2 . With this conjecture the concept of a single universal Pomeron trajectory becomes obsolete for hard scattering processes. It has become customary, however, to introduce an effective Pomeron trajectory $\alpha(t) = \alpha_0 + \alpha't$, where the intercept α_0 can be calculated within certain QCD models (see for example [20] for a review).

In photoproduction of J/ψ mesons the mass $M_{J/\psi}$ may serve as a hard scale and in electroproduction both $M_{J/\psi}$ and Q^2 . A third hard scale may be provided by a sufficiently large momentum transfer $|t|$ at the proton vertex [13, 14]. In the presence of a hard scale QCD factorisation methods (e.g. collinear factorisation, k_T factorisation) may be applied. Factorisation allows the separation of the scattering amplitude into a perturbative hard scattering coefficient function and non-perturbative quantities, such as the input gluon density for the proton and the vector meson wave function.

Early pQCD predictions, for example [21], assume that the two exchanged gluons have the same longitudinal momentum fraction x with respect to the proton, where $x \simeq (Q^2 + M_\psi^2)/(Q^2 + W_{\gamma p}^2)$, and that each of the quarks making up the J/ψ meson carries half of the photon momentum. Such models correspond to a leading approximation in $\log 1/x$, and at high energies the cross section depends on the square of the gluon density within the proton. More recently generalised or “skewed” parton distributions have been considered, where the two gluons have different fractional momenta [22–26].

The data presented here are compared with a pQCD model by Martin, Ryskin and Teubner (MRT [26]) which is based on k_T factorisation and uses a parton-hadron duality ansatz avoiding the large uncertainties from the poorly known J/ψ meson wave function. In this model, effects beyond the leading logarithmic approximation in $\log Q^2$ are included at the amplitude level, requiring an integration over the transverse momenta of the two gluons and hence the use of unintegrated gluon distributions. In the MRT calculations these distributions are derived [25] from the conventional integrated parton distributions¹, as extracted from inclusive deep-inelastic scattering. The skewing effects are estimated independently by applying a factor to the amplitude [27]. Since these calculations only apply to the imaginary part of the scattering amplitude, dispersion relations are used to estimate the effects of the real part. In the parton-hadron duality approach the correct spin-parity state ($J^P = 1^{--}$) of the $c\bar{c}$ pair is projected out by using the appropriate rotation matrices in the integrals over the resonance mass region. Since the choice of the mass range in the integration is arbitrary to some extent, the normalisation of the cross sections is predicted with limited accuracy. The overall normalisation contains additional uncertainties due to missing higher order corrections. The approximations used are however believed to have little influence on the $W_{\gamma p}$ and Q^2 dependences of the cross sections [28]. Predictions are provided both in the photoproduction and electroproduction regimes.

The calculations by Frankfurt, McDermott and Strikman (FMS [9]) are based on the dipole approach. Here the exchanged photon turns into a $q\bar{q}$ pair long before the interaction with the proton. A leading logarithmic approximation for the interaction of this $q\bar{q}$ pair, described as a small transverse-size dipole, is used. For the interaction with the proton two-gluon exchange is assumed. In addition the effect of a running quark mass, a $W_{\gamma p}$ dependent slope of the exponential t distribution, and generalised gluon distributions are considered in this calculation. Similarly to the MRT calculations the model does not provide an accurate normalisation of the cross section. Predictions are only available for photoproduction.

¹In this model the unintegrated gluon distribution is determined from the derivative of the standard gluon distribution with respect to $\log Q^2$, i.e. essentially from the second derivative of the proton structure function $F_2(x, Q^2)$ with respect to $\log Q^2$, which in the kinematic region of the J/ψ analysis, at low x and Q^2 , is not well measured at HERA yet.

3 Data Analysis

The data were recorded with the H1 detector in the years 1999 and 2000 when HERA was operated with electrons or predominantly with positrons² of 27.5 GeV and protons of 920 GeV. The J/ψ mesons are detected via their decays into $\mu^+\mu^-$ or e^+e^- pairs. They are selected from data corresponding to an integrated luminosity of 55 pb⁻¹.

3.1 The H1 Detector

The H1 detector is described in detail in [29]. Charged particles are detected in the central and forward³ tracking detectors (CTD and FTD), which consist of drift and proportional chambers that provide a polar angle coverage between 7° and 165°. Tracks at large θ are detected in the backward silicon tracker (BST [30], 165° < θ < 175°). The central liquid argon (LAr) [29] and backward lead scintillator (SpaCal) calorimeters [31, 32] cover the polar angle regions 4° < θ < 153° and 153° < θ < 177.5°, respectively. For $Q^2 \gtrsim 2$ GeV² the scattered positron is detected in the SpaCal, while the decay electrons from the J/ψ meson are identified in the LAr and SpaCal calorimeters. Muons are identified as minimum ionising particles in the LAr calorimeter or in the instrumented iron return yoke of the solenoidal magnet which surrounds the central detector (central muon detector, CMD, 4° < θ < 171°).

Dissociated proton states Y with masses $M_Y \gtrsim 1.6$ GeV may, after a secondary interaction, be measured in a set of detectors in the forward direction. These are the proton remnant tagger (PRT), an array of scintillators covering 0.06° < θ < 0.17°, the drift chambers of the forward muon detector (FMD) [33] closest to the beam interaction region in the angular range 3° < θ < 17° and the forward region of the LAr calorimeter (θ < 10°).

H1 uses a multi-stage trigger system. At level 1 signals from the CTD, SpaCal, and CMD are used to obtain the present data sets. At level 2 information from these detectors and the LAr calorimeter is used in neural network algorithms [34].

The luminosity is determined from the rate of Bethe Heitler events.

3.2 Kinematics

The kinematics of the process $ep \rightarrow epJ/\psi$ are described by the following variables: the square of the ep centre of mass energy $s = (p + k)^2$; the negative four-momentum transfer squared at the lepton vertex $Q^2 = -q^2 = -(k - k')^2$; the four-momentum transfer squared at the proton vertex $t = (p - p')^2$ and the inelasticity $y = (p \cdot q)/(p \cdot k)$. The four-momenta k , k' , p , p' and q refer to the incident and scattered positron, the incoming and outgoing proton (or dissociated system Y) and the exchanged photon, respectively. The centre of mass energy of the photon-proton system $W_{\gamma p}$ is given by $W_{\gamma p}^2 = (p + q)^2 = ys - Q^2$ neglecting the proton mass.

²Hereafter the term ‘positron’ is used for all lepton beam particles, whereas ‘electron’ is used for both electrons and positrons from J/ψ decays.

³The positive z -axis is defined by the proton beam direction. The polar angle θ is measured with respect to the z axis and $\theta < 90^\circ$ is called the ‘forward’ direction.

In electroproduction the event kinematics are reconstructed using the double angle method [35],

$$y = \frac{\sin \theta_e (1 - \cos \theta_\psi)}{\sin \theta_\psi + \sin \theta_e - \sin(\theta_e + \theta_\psi)}$$

$$Q^2 = 4E_e^2 \frac{\sin \theta_\psi (1 + \cos \theta_e)}{\sin \theta_\psi + \sin \theta_e - \sin(\theta_e + \theta_\psi)}.$$

Here E_e is the energy of the incident positron and θ_ψ and θ_e are the polar angles of the J/ψ meson and the scattered positron, respectively. The variable t is calculated as $t \simeq -(\vec{p}_{t,\psi} + \vec{p}_{t,e})^2$, where $\vec{p}_{t,\psi}$ is the transverse momentum of the J/ψ meson candidate and $\vec{p}_{t,e}$ that of the outgoing positron.

In photoproduction, where the positron is not observed in the central detector, y is reconstructed via $y = (E - p_z)_\psi / (2E_e)$ [36], where E and p_z denote the energy and the longitudinal component of the momentum of the J/ψ meson. The variable t is approximated as $t \simeq -p_{t,\psi}^2$ (see also the section on $d\sigma/dt$ below).

3.3 Monte Carlo Simulation

Monte Carlo simulations are used to calculate acceptances and the efficiencies for triggering, track reconstruction, event selection and lepton identification.

The elastic J/ψ signal events are generated using the program DIFFVM [37] which is based on the Vector Dominance Model and permits separate variation of the dependence on $W_{\gamma p}$, t and Q^2 . The parameters are iteratively adjusted to those of the present measurements. DIFFVM is also used to generate J/ψ production with proton dissociation. A mass dependence of $d\sigma/dM_Y^2 \propto f(M_Y^2) M_Y^{-\beta}$ is implemented, where $f(M_Y^2) = 1$ for $M_Y^2 > 3.6 \text{ GeV}^2$. At lower M_Y^2 the function $f(M_Y^2)$ takes into account the production of excited nucleon states. The decay angular distributions of the J/ψ meson are simulated assuming s -channel helicity conservation. For electroproduction, radiative corrections are included using the generator HERACLES [38], where contributions up to order α_{QED}^3 are taken into account.

The non-resonant background is estimated using the generators LPAIR [39], which simulates the process $\gamma\gamma \rightarrow \ell^+\ell^-$ and COMPTON [40] for the QED Compton process $ep \rightarrow e\gamma p$. Cross checks with the generator GRAPE [41] did not show significant deviations from the results of LPAIR in the region of the present analysis.

For all processes, detector effects are simulated in detail with the GEANT program [42]. The detector response including trigger efficiencies is tuned using independent data. Remaining differences are included in the systematic errors. The simulated events are passed through the same reconstruction software as the data.

3.4 Event Selection

Elastic J/ψ events are selected by requiring two muons or two electrons and, in the case of electroproduction, a scattered positron candidate. For photoproduction the absence of any such

candidate is required. As described in table 1 four data sets are defined covering different regions of Q^2 and $W_{\gamma p}$ and corresponding to different signatures of the J/ψ decay leptons.

For data set I (electroproduction) the scattered positron must be detected with an energy of at least 12 GeV in the SpaCal and the reconstructed value of Q^2 must be within $2 < Q^2 < 80 \text{ GeV}^2$. To suppress photoproduction background and to reduce the fraction of events with initial state QED radiation, events are rejected if $\sum(E - p_z) < 45 \text{ GeV}$, where the sum runs over all final state particles including the scattered positron. Neglecting radiative effects this variable is expected to be twice the incident positron energy due to longitudinal momentum conservation.

For the selection of photoproduction events (data sets II–IV) the absence of any candidate for the scattered positron is required, restricting the accepted range of negative four-momentum transfer squared Q^2 to below about 1 GeV^2 , with $\langle Q^2 \rangle = 0.05 \text{ GeV}^2$.

Data sets I and II ($40 < W_{\gamma p} < 160 \text{ GeV}$) contain $J/\psi \rightarrow \mu^+ \mu^-$ events. Exactly two oppositely charged particles must be present in the CTD, with transverse momenta (with respect to the beamline) $p_t > 0.8 \text{ GeV}$. A reconstructed vertex within $\pm 40 \text{ cm}$ of the z coordinate of the nominal beam interaction point is required. At least one particle must be identified as a muon in the central calorimeter or in the CMD. For data set II background from cosmic ray muons is rejected using an acollinearity cut as well as timing information from the CTD. Further details of this analysis may be found in [43].

Data sets III and IV are selected to cover photoproduction at high values of $W_{\gamma p}$, which are related to large polar angles of the J/ψ decay leptons. The J/ψ decay into $e^+ e^-$ pairs is used. Data set III ($135 < W_{\gamma p} < 235 \text{ GeV}$) requires one decay electron to be measured in the CTD coming from within $\pm 40 \text{ cm}$ of the nominal beam interaction point and one in the

Data set	I	II	III	IV
Kinematic region	Electroproduction	Photoproduction		
Q^2 range [GeV^2]	2 – 80	< 1		
$\langle Q^2 \rangle$ [GeV^2]	8.9	0.05		
$W_{\gamma p}$ [GeV]	40 – 160		135 – 235	205 – 305
$ t $ [GeV^2]	< 1.2			
Decay channel	$J/\psi \rightarrow \mu^+ \mu^-$		$J/\psi \rightarrow e^+ e^-$	
Lepton signature	Track-Track		Track-Cluster	Cluster-Cluster
Lepton polar angle region [$^\circ$]	20 – 160		$\theta_1 : 80 - 155$ $\theta_2 : 160 - 177$	$\theta_1 : 160 - 174$ $\theta_2 : 160 - 175.5$
Lepton energy [GeV]	$p_t > 0.8$		$p_{t,1} > 0.7, p_1 > 0.8$ $E_2 > 4.2$	$E_{1,2} > 4.2$ $\max(E_1, E_2) > 6$
Elastic selection	No signal in forward detectors			
$\int L dt$ [pb^{-1}]	54.79		30.26	26.90

Table 1: Summary of the most important event selection criteria for the four different data sets together with the corresponding integrated luminosities.

backward calorimeter SpaCal. The selected polar angle regions are given in table 1. The electron measured in the CTD must have a momentum $p_1 > 0.8$ GeV and a transverse momentum $p_{t,1} > 0.7$ GeV and must be identified by a matching electromagnetic energy deposition in the central calorimeter. The other electron is selected by requiring a cluster in the SpaCal with an energy $E_2 > 4.2$ GeV. Data set IV ($185 < W_{\gamma p} < 305$ GeV) requires both electrons to be detected as energy clusters in the SpaCal with energies $E_{1,2} > 4.2$ GeV and the more energetic cluster to be above 6 GeV. At least one electron must be in the acceptance region of the BST and every electron in the BST acceptance region must be validated by a BST track from the nominal interaction point. This requirement rejects most of the non-resonant background from Compton scattering. In both data sets III and IV the energy in the SpaCal outside the selected electron cluster(s) must be negligible. Further details of this analysis may be found in [44].

In order to suppress background from proton dissociative or inelastic J/ψ production, no additional tracks are allowed in the CTD or FTD and the selected events are required to have no significant signals in the forward detectors (PRT, FMD and LAr). The fraction of proton dissociation is further suppressed by limiting t to the range $|t| < 1.2$ GeV², where elastic processes are dominant. These requirements reject most of the proton dissociative background. The remaining fraction is 14% on average, ranging from 8% at $|t| \approx 0$ to 35% at $|t| \approx 1.2$ GeV². It is corrected for using the MC simulation, which is tuned to give a good description of the forward detectors. A further correction is applied to account for $\psi(2S)$ decays into J/ψ and neutral mesons. This correction is estimated to be 4% for data sets I and II and approximately 2% in sets III and IV, where the neutral decays are partly rejected by the cut on the energy in the SpaCal.

Triggers based on muon and track signatures from the decay leptons are used for data sets I and II. For data set I a trigger signal is also derived from the scattered positron. The triggers for data sets III and IV are based on signals due to the J/ψ decay electrons from the SpaCal and the CTD (set III). In addition the triggers for data sets II-IV use second level triggers based on neural network algorithms.

Figure 2 shows the two-lepton invariant mass distributions for the four data sets. The shapes of the J/ψ signal peaks reflect the usage of different detectors with different resolutions and a different response to electrons, muons and photons. The signal of data set III shows a tail towards low masses due to radiative energy losses of the electron reconstructed in the tracking detector. In all data sets the non resonant background below the J/ψ signal peaks is dominated by $\gamma\gamma \rightarrow \ell^+\ell^-$, where one photon originates from each of the positron and the proton. At high $W_{\gamma p}$ a potential source of background is Compton scattering $ep \rightarrow e\gamma p$ where the final state electron and photon can form an invariant mass of the same order as the J/ψ mass. It is efficiently suppressed by the BST track requirements explained above. In addition the BST tracks lead to an improved mass resolution in data set IV.

The number of J/ψ events is determined in each analysis bin by a fit of the sum of a signal and a background function to the dilepton mass distribution. For data sets I and II ($J/\psi \rightarrow \mu^+\mu^-$) the signal shape is a Gaussian function, and the background is fitted using a power law distribution. For the signal in data set III ($J/\psi \rightarrow e^+e^-$) the radiative tail is taken into account by fitting a modified Gaussian distribution, $f(M_{ee}) \propto \frac{1}{\sigma'} \exp(-(M_{ee} - \mu)^2/(2\sigma'))$ where $\sigma' = (\sigma + r(|M_{ee} - \mu| - M_{ee} + \mu))^2$. Here μ and σ denote the peak position and the standard deviation and r parameterises the contribution of the radiative tail. In data set IV

($J/\psi \rightarrow e^+e^-$) a single Gaussian function is adequate to describe the signal. In data sets III and IV the shape of the background is found to depend strongly on $W_{\gamma p}$. The shapes are reasonably well described by the predicted shapes of the Monte Carlo simulations LPAIR and COMPTON, which are therefore used in the fit.

Data and MC simulation are compared in figure 3. Each row corresponds to one of the four data sets. The selected events from a mass window around the nominal J/ψ mass (± 0.2 GeV in data sets I and II, ± 0.3 GeV in data set IV and $2.6 < M_{ee} < 3.4$ GeV for data set III) are shown before applying the cuts on the forward detectors. For data sets I and II the non-resonant background, which is small in this kinematic region, has been subtracted and the data are described by a combination of DIFFVM for elastic and proton dissociative J/ψ production. For data sets III and IV the selected events are shown but without subtracting the non resonant background. The data are seen to be reasonably well described by a sum of simulations for elastic and proton dissociative J/ψ production (DIFFVM), $\gamma\gamma \rightarrow e^+e^-$ (LPAIR) and $ep \rightarrow e\gamma p$ (COMPTON).

3.5 Systematic Uncertainties

The systematic uncertainties on the cross sections are dominated by detector effects which are not perfectly modelled in the Monte Carlo simulation. Most uncertainties are obtained by comparisons of data with simulation after tuning the detector simulation with independent data sets. The uncertainties on the measured cross sections are then estimated by variations of the simulation. In the following the main sources of the uncertainties are summarised and typical values are given for the uncertainty on the total cross section.

- The uncertainty due to the track reconstruction efficiency in the CTD is 1% per track. The track information from the BST has two sources of uncertainty: coherent signal losses (3.0%) and track reconstruction efficiency (1.5%).
- The uncertainty on the lepton identification efficiency leads to a cross section uncertainty of 1.5% for muons and 2% for electrons measured in the CTD. The uncertainty on the energy measurement of the decay electrons in the backward calorimeter is estimated to vary linearly from 2.7% at 3 GeV to 0.5% at 27.5 GeV from an analysis of Compton scattering [45]. The resulting uncertainties on the cross sections vary from 1% to 7%, depending on $W_{\gamma p}$. A small additional uncertainty for data set IV arises due to an uncertainty of 0.3 mrad in the reconstruction of the polar angle of the decay electrons in the BST, leading to a $W_{\gamma p}$ dependent cross section uncertainty of 1 – 3%.
- The uncertainties of the trigger efficiencies are determined to be 1.6%, 5%, 6.5% and 5% for data sets I to IV, respectively.
- The separation of elastic events from proton dissociation leads to a systematic uncertainty of 4 – 6% due to the modelling of the response of the forward detectors, with a small dependence on $W_{\gamma p}$ and $|t|$. The error due to the simulation of the dependence of the cross section on M_Y was found to be negligible by comparison.

- The uncertainty in the modelling of the z position of the interaction region affects the $W_{\gamma p}$ dependence of the cross section and is found to be 1% on average for data sets I and II, 0.5 – 2.6% for III and 2.0% for IV.
- Varying the methods of determination of the number of signal events (e.g. by using a counting method instead of fits, or by changing the shapes of the background functions), results in a 1% uncertainty for data sets I and II ($\mu^+\mu^-$). For data sets III and IV (electrons) an uncertainty between 3% and 6% is estimated, which is due to the uncertainties in the signal and background shapes.
- For the electroproduction sample, an additional uncertainty of 4% is estimated which covers uncertainties in the reconstruction of the energy and angle of the scattered positron.
- Other sources of systematic uncertainties are the luminosity measurement (1.5%), the J/ψ branching ratio (1.7%) and the $\psi(2S)$ background (0.5% for sets I and II, 1.5% on average for III and IV).

The systematic uncertainties are calculated in each analysis bin and the total uncertainty is obtained by adding all individual contributions in quadrature. The average values for the total systematic uncertainties on the cross sections are 8%, 9%, 10% and 11% for the data sets I to IV, respectively. The correlated part of the error, which affects all bins equally, is estimated to be approximately 5% and is not included in subsequent fits unless mentioned otherwise.

4 Results

Cross sections are calculated for the individual data sets I–IV using the number N of selected events after correcting for non resonant, proton dissociative and $\psi(2S)$ backgrounds as described in the previous section. The efficiencies A for the event selection are in general determined from the MC simulation. In the equivalent photon approximation the γp cross section is given by:

$$\sigma(\gamma p \rightarrow J/\psi p) = \frac{N}{A \cdot BR \cdot \mathcal{L} \cdot \Phi_\gamma}. \quad (1)$$

Here Φ_γ [46] denotes the photon flux in the Q^2 and $W_{\gamma p}$ range considered, \mathcal{L} the integrated luminosity and BR the branching ratio for the decay of the J/ψ mesons⁴.

Note that this cross section corresponds to $\sigma_{\gamma p} = \sigma_{\gamma p}^T + \varepsilon \sigma_{\gamma p}^L$, where $\sigma_{\gamma p}^T$ and $\sigma_{\gamma p}^L$ are the cross sections for transversely and longitudinally polarised photons, respectively, and ε is the polarisation parameter of the virtual photon⁵. The parameter ε depends only on the kinematics, $\varepsilon = (1 - y)/(1 - y + \frac{1}{2}y^2)$. In the kinematic range of the present analysis ε is generally above 0.95 with $\langle \varepsilon \rangle = 0.993$. Cross sections are given at ‘bin centres’, $\langle W_{\gamma p} \rangle$, $\langle Q^2 \rangle$ and $\langle t \rangle$, which are determined taking into account the measured $W_{\gamma p}$, Q^2 and t dependences.

⁴Branching fractions $(5.88 \pm 0.10)\%$ and $(5.93 \pm 0.10)\%$ [47] are used for $J/\psi \rightarrow \mu^+\mu^-$ and e^+e^- , respectively.

⁵The present results will be compared with results from the ZEUS collaboration [16], where $\sigma_{\gamma p}^T + \sigma_{\gamma p}^L$ is extracted. In the present kinematic region the difference is however small compared with the measurement errors.

4.1 Q^2 Dependence

The cross sections for elastic J/ψ production as a function of Q^2 at $W_{\gamma p} = 90$ GeV are listed in table 2 and shown in figure 4a. The photoproduction point is obtained from the fit described in the next section.

A phenomenological fit of the form $\sigma_{\gamma p} \propto (M_\psi^2 + Q^2)^{-n}$ to the H1 data yields a value of $n = 2.486 \pm 0.080(\text{stat.}) \pm 0.068(\text{syst.})$. This result confirms, with smaller errors, the Q^2 dependence observed previously by H1 [11]. The quality of the fit is good ($\chi^2/\text{ndf} = 0.5$). Recent results from the ZEUS collaboration [6, 16] are also shown in figure 4a, which agree well with the present data in the entire range of Q^2 .

In figure 4b the pQCD calculations ‘MRT’ of Martin et al. [26] are compared with the fit result quoted above. Results with four different gluon distributions (CTEQ6M [48], MRST02 [49], H1QCDFIT [50] and ZEUS-S [51]) derived from global fits to current inclusive F_2 measurements and other data are shown. A normalisation factor is determined individually for each prediction by comparing with the data across the complete Q^2 range. The different factors, which are mainly given by the photoproduction measurement, are between 1.5 and 2.8. The theoretical predictions of the shape of the Q^2 dependence are consistent with the fit to the data within the experimental uncertainties, which are shown as a grey band in figure 4b.

4.2 $W_{\gamma p}$ Dependence

The γp cross section for elastic J/ψ production is presented as a function of $W_{\gamma p}$ in figures 5a and 6a and in tables 3 and 4 for photoproduction and electroproduction, respectively.

In figure 5a the photoproduction data are shown with the result of a fit of the form $\sigma_{\gamma p} \propto W_{\gamma p}^\delta$. Separate relative normalisation factors for the three data sets are additional fit parameters which take into account the correlated systematic uncertainties. The fit yields a value of $\delta = 0.75 \pm 0.03 \pm 0.03$. The first error is obtained using only the statistical uncertainties in the fit while the second one reflects the systematic uncertainties. The fit result is in agreement with our previous result [4]. Similar data from the ZEUS collaboration [6] (also shown in figure 5a) agree well with the present data.

A comparison with theoretical predictions is shown in figure 5b, where the ratio of theory to the fit result is shown. The uncertainty of the fit result is indicated by the grey band. The MRT predictions are normalised using the factors obtained from the Q^2 distributions. The same four gluon distributions are used to calculate the respective unintegrated skewed gluon distributions which are required by MRT. The $W_{\gamma p}$ dependence is observed to be quite sensitive to the shape of the gluon distribution⁶. While the results based on the gluon distributions CTEQ6M and ZEUS-S describe the shape of the data well, the gluon distribution from the H1 fit to inclusive data leads to a steeper $W_{\gamma p}$ dependence and the one from MRST02 to a flatter $W_{\gamma p}$ dependence than is observed. The dipole model result FMS [9] based on the CTEQ4L [52] gluon density is somewhat too steep. Note, however, that these observations are based on the central values of the respective gluon distributions and do not take into account their uncertainties. The kinematic range used in the MRT calculations extends to lower values of Bjorken x and Q^2

⁶For a detailed discussion of the sensitivity and the uncertainties of the model assumptions see [28].

than was available in the inclusive data used for the determination of the gluon densities and an extrapolation to very low values of Q^2 is performed.

In figure 6a the electroproduction cross section is shown in three bins of Q^2 ($2 < Q^2 < 5 \text{ GeV}^2$, $5 < Q^2 < 10 \text{ GeV}^2$ and $10 < Q^2 < 80 \text{ GeV}^2$). Data from the ZEUS experiment [16], which are shifted to the present bin centres using the Q^2 dependence measured by ZEUS, are in agreement. In figure 6a the results from MRT based on the gluon density CTEQ6M using the same normalisation factor as above are also shown and give a reasonable description of the data.

The $W_{\gamma p}$ dependence is found to be similar to that obtained in photoproduction. When parameterised in the form $W_{\gamma p}^\delta$, the fits to the H1 electroproduction data yield δ values which are compatible with photoproduction within the rather large experimental errors (see table 5). The fitted values for δ describing the $W_{\gamma p}$ dependence of elastic J/ψ production from this analysis and from [6, 16] are displayed in figure 6b as a function of Q^2 . Within the present experimental accuracy no dependence on Q^2 is observed.

4.3 Differential Cross Sections $d\sigma/dt$

The t dependence of the elastic cross section for J/ψ meson production is studied in the range $40 < W_{\gamma p} < 160 \text{ GeV}$ for different Q^2 bins. The differential cross sections $d\sigma/dt$ as derived from data sets I and II are listed in table 6 and shown in figure 7a with fits of the form $d\sigma/dt \propto e^{bt}$. The resulting b values (table 5) for electroproduction are systematically lower than the value for photoproduction but are compatible within the errors.

In the context of developing the calculations using generalised parton densities, Frankfurt and Strikman [8] have proposed an alternative t dependence. It is based on a dipole function with a t dependent two-gluon form factor, leading to $d\sigma/dt \propto (1 - t/m_{2g}^2)^{-4}$. In a fit to the photoproduction data the two-gluon invariant mass m_{2g} is left as a free parameter. A value of $m_{2g} = (0.679 \pm 0.006 \pm 0.011) \text{ GeV}$ is obtained with $\chi^2/\text{ndf} = 5.5$ compared to $\chi^2/\text{ndf} = 0.25$ for the exponential function. The dipole form is thus strongly disfavoured by the data.

For photoproduction, the measurement of the t dependence has been extended to significantly higher $W_{\gamma p}$ than in our previous publication [4] using data sets III ($135 < W_{\gamma p} < 235 \text{ GeV}$) and IV ($205 < W_{\gamma p} < 305 \text{ GeV}$). Due to the reconstruction of the J/ψ electrons via calorimeter signals the resolution in $p_{t,\psi}^2$, which is used to approximate t , is worse than in the track based measurements. The differential cross sections $d\sigma/dt$ are obtained using an unfolding procedure [53]. The results (last two lines in table 7) are shown in figures 7b and c with exponential fits, which describe the data well. The resulting b values are listed in table 10 and are discussed further in the following section.

4.4 Effective Pomeron Trajectories

In models based on Regge phenomenology and Pomeron exchange, the energy dependence of the elastic cross section follows a power law:

$$\frac{d\sigma}{dt} = \left. \frac{d\sigma}{dt} \right|_{t=0, W_{\gamma p}=W_0} \cdot e^{b_0 t} \left(\frac{W_{\gamma p}}{W_0} \right)^{4(\alpha(t)-1)}, \quad (2)$$

where $\alpha(t) = \alpha_0 + \alpha' t$ describes the exchanged trajectory and b_0 and W_0 are constants. Equation 2 relates the dependence of the differential cross section on t to that on $W_{\gamma p}$ by

$$\frac{d\sigma}{dt}(t) \propto e^{(b_0 + 4\alpha' \ln(W_{\gamma p}/W_0))t}. \quad (3)$$

Here only t dependent terms are kept. In hard interactions, where Regge phenomenology with a single universal Pomeron may no longer be applicable, an ‘effective Pomeron trajectory’ [20] is nevertheless often extracted in order to describe the dependence of the differential cross sections on $W_{\gamma p}$ and t . For the determination of this effective trajectory, a double differential analysis is performed in which the differential cross section $d\sigma/dt$ is measured in bins of $W_{\gamma p}$ and t . The measurements are displayed in figures 8a and b for photoproduction and electroproduction, respectively (tables 7 and 8). First, one-dimensional fits of the form $W_{\gamma p}^{4(\alpha(\langle t \rangle)-1)}$ to the cross sections in each $|\langle t \rangle|$ bin are performed. The results, which are listed in table 9 and displayed as solid lines in figures 8a and b, describe the data well. In figures 9b and c the one-dimensional fit results for $\alpha(t)$ are compared with recent results [6, 16] from the ZEUS collaboration, which are in good agreement.

A two-dimensional fit of the function given in equation 2 to the data yields values for b_0 , α_0 and α' . The parameter W_0 is arbitrarily chosen to be 90 GeV; the fit result does not depend on this choice. As described before, different normalisations are allowed for the different data sets in the fit. Figure 9a shows the result of the two-dimensional fit for $\alpha(t)$ as solid and dashed lines for photoproduction and electroproduction, respectively. Error bands corresponding to one standard deviation are shown, taking the correlation between α_0 and α' into account. The results for $\alpha(\langle t \rangle)$ from the one-dimensional fits are shown as points with error bars for comparison. Good internal consistency is observed.

The results of the two-dimensional fits are listed in the following table.

Q^2 [GeV ²]	b_0 [GeV ⁻²]	α_0	α' [GeV ⁻²]
$\lesssim 1$	$4.630 \pm 0.060^{+0.043}_{-0.163}$	$1.224 \pm 0.010 \pm 0.012$	$0.164 \pm 0.028 \pm 0.030$
$2 - 80$	$3.86 \pm 0.13 \pm 0.31$	$1.183 \pm 0.054 \pm 0.030$	$0.019 \pm 0.139 \pm 0.076$

Here the first errors are statistical and the second reflect the systematic uncertainties.

The $W_{\gamma p}$ dependence of the cross section is predominantly determined by α_0 and the fit values lead to a $W_{\gamma p}$ dependence very similar to the parameterisation with δ discussed above. The parameter α' relates the t and $W_{\gamma p}$ dependences and if non-zero leads to the ‘shrinkage’ of the diffractive peak. For photoproduction α' is larger than zero by four standard deviations and is two standard deviations below the value of 0.25 GeV⁻² obtained for the soft Pomeron in [54]. For electroproduction α' is compatible with 0, which matches the expectation in [20], but due to the errors α' is also compatible with the value measured for photoproduction.

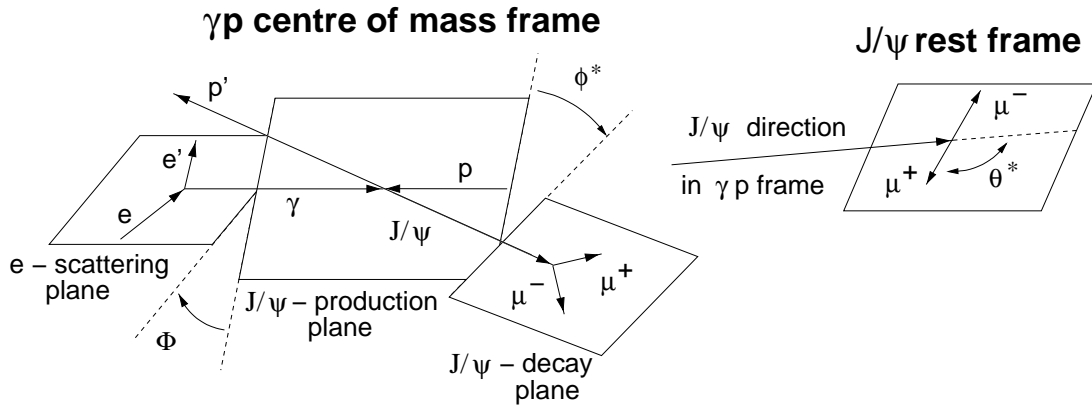
Alternatively the value of α' can be measured using the dependence of the t slope parameter on $W_{\gamma p}$, using $b(W_{\gamma p}) = b_0 + 4\alpha' \ln(W_{\gamma p}/W_0)$. Exponential fits of the form e^{bt} to the measured differential cross sections $d\sigma/dt$ in bins of $W_{\gamma p}$ are performed and the resulting values for b are displayed in figure 10a and b and listed in table 10 for photoproduction and electroproduction.

For photoproduction the b values are seen to increase with $W_{\gamma p}$. These b values are independent of normalisation uncertainties between data sets. The curves in figure 10a and b show the corresponding result $b(W_{\gamma p})$ from the two-dimensional fit described above.

In figure 10a photoproduction results for the slope parameter from the ZEUS experiment [6] in a similar kinematic region are also shown. They show a similar dependence on $W_{\gamma p}$ but are on average 0.5 GeV^{-2} lower. This difference in the absolute size of b may be due to differences in the handling of the background from proton dissociative events, which has a much shallower b slope than for the elastic case (1.6 GeV^{-2} [13]).

4.5 Helicity Studies

The assumption that the J/ψ meson observed in the final state keeps the helicity of the photon is referred to as s -channel helicity conservation (SCHC). This assumption can be tested by measurements of the angles in the production and decay of the J/ψ meson. If SCHC holds, the angular analysis leads to a separation of the cross sections due to longitudinally and transversely polarised photons which are both predicted in the MRT calculations.



Three angles are defined, which are illustrated in the figure above. θ^* is the polar angle of the decay muon with the charge of the beam lepton in the J/ψ rest frame. $\theta^* = 0^\circ$ corresponds to the flight direction of the J/ψ in the γp centre of mass frame. ϕ^* is the angle between the J/ψ production plane, defined by the exchanged photon and the J/ψ meson, and the decay plane in the γp centre of mass frame. Φ is the angle between the scattering plane of the beam lepton and the J/ψ production plane. The angle Φ can only be measured when the scattered electron is observed, i.e. for electroproduction. In the case of SCHC and natural parity exchange, the angular distributions of the J/ψ production and decay are functions of $\cos \theta^*$ and $\Psi = \phi^* - \Phi$ only [55].

The angular distributions are expected to be similar for elastic and proton dissociative processes. This expectation is verified within the present statistical accuracy. Therefore, in order to increase the statistics, the cross sections differential in the angles are derived using a data set, which includes proton dissociative events in addition to data sets I and II. The selection of proton dissociative events is similar to that for data sets I and II (section 3.4 and table 1), but now a signal in one of the forward detectors is required and one additional track is allowed with

$\theta < 20^\circ$. Non-diffractive events are rejected by requiring $z > 0.95$, where $z = E_{J/\psi}/E_\gamma$ in the proton rest frame. Furthermore, an increased t range, $|t| < 5 \text{ GeV}^2$, is allowed, since the proton dissociative J/ψ cross section shows a flatter t dependence, with an exponential slope of about 1.6 GeV^{-2} [13].

In the present analysis, differential cross sections for the four angles are used to measure combinations of seven of the 15 spin-density matrix elements, which describe the spin structure of the interaction completely⁷. The measured angular distributions and their dependence on the spin-density matrix elements $r_{\lambda(\gamma)\lambda(\psi)}^{ik}$ are [55]:

$$\frac{d\sigma}{d\cos\theta^*} \propto 1 + r_{00}^{04} + (1 - 3r_{00}^{04}) \cos^2\theta^* \quad (4)$$

$$\frac{d\sigma}{d\phi^*} \propto 1 + r_{1-1}^{04} \cos(2\phi^*) \quad (5)$$

$$\frac{d\sigma}{d\Psi} \propto 1 - \varepsilon r_{1-1}^1 \cos(2\Psi) \quad (6)$$

$$\frac{d\sigma}{d\Phi} \propto 1 - \varepsilon (r_{00}^1 + 2r_{11}^1) \cos 2\Phi + \sqrt{2\varepsilon(1+\varepsilon)} (r_{00}^5 + 2r_{11}^5) \cos \Phi. \quad (7)$$

Here ε is the polarisation parameter of the virtual photon.

Figures 11a and b show the differential γp cross sections $d\sigma/d\cos\theta^*$ and $d\sigma/d\phi^*$ in four bins of Q^2 . Figures 11c and d show the differential cross sections $d\sigma/d\Psi$ and $d\sigma/d\Phi$ in three bins of Q^2 . The results of fits of equations 4, 5, 6 and 7 are shown as full lines. In the fits, the spin-density matrix elements or the combinations $r_{00}^1 + 2r_{11}^1$ and $r_{00}^5 + 2r_{11}^5$ for equation 7 are free parameters. In figure 11b and d results from a fit assuming SCHC are also shown.

The spin density matrix elements, which are determined by the fits, are shown in figures 12a–e as functions of Q^2 (tables 11 and 12). The analysis is also performed in bins of $|t|$ and the resulting spin density matrix elements are displayed in figures 12f–j (tables 13 and 14) as functions of $|t|$.

Results from the ZEUS experiment [5, 6, 15, 16] are also shown in figures 12a, b, c and f, which are in good agreement with the present results. In figures 12b, d, e, g, i and j the expectation from SCHC, namely 0, matches the data well. SCHC yields a relation between two spin density matrix elements: $r_{1-1}^1 = (1 - r_{00}^{04})/2$. This is observed to be fulfilled within errors.

In the case of SCHC, the matrix element r_{00}^{04} provides a direct measurement of R , the ratio of the cross sections for longitudinal and transverse polarised photons, σ^L and σ^T , respectively:

$$R = \frac{\sigma^L}{\sigma^T} = \frac{1}{\varepsilon} \frac{r_{00}^{04}}{1 - r_{00}^{04}}.$$

The values of R are presented in figure 13a and in table 11. For comparison the prediction from MRT [26] is shown, which depends only weakly on the gluon density. In figure 13a the

⁷Spin density matrix elements $r_{\lambda(\gamma)\lambda(\psi)}^i$ or $r_{\lambda(\gamma)\lambda(\psi)}^{ik}$ are linear combinations of the transition amplitudes $T_{\lambda(\gamma)\lambda(\psi)}^{i,k}$ from a photon of helicity $\lambda(\gamma)$ to a J/ψ of helicity $\lambda(\psi)$.

gluon density from CTEQ6M is chosen with the normalisation as before, which gives the best description of the Q^2 and $W_{\gamma p}$ dependences of the cross sections. The prediction is somewhat above the data but still describes the Q^2 dependence reasonably well. Similar results from [6, 16] agree also with the present data.

The values of R can be used to derive the cross sections σ^L and σ^T using the relationship $\sigma_{\gamma p} = \sigma_{\gamma p}^T + \varepsilon \sigma_{\gamma p}^L$. The results are shown in figure 13b as a function of Q^2 . σ^T dominates at low Q^2 , while at $Q^2 \sim M_\psi^2$ both σ^T and σ^L are of similar magnitude. The MRT predictions are compared with the data using different gluon density parameterisations. The differences between the predictions are not very large. All gluon density parameterisations give a reasonable description of the data, although σ_L is somewhat above the data for $Q^2 \gtrsim 3 \text{ GeV}^2$.

In brief, the helicity studies show consistency with SCHC within experimental errors. The ratio of cross sections for longitudinally and transversely polarised photons is extracted and its Q^2 dependence is found to be reasonably described by the MRT calculations.

5 Summary

New measurements are presented of elastic J/ψ photoproduction and electroproduction in the ranges $40 < W_{\gamma p} < 305 \text{ GeV}$ and $40 < W_{\gamma p} < 160 \text{ GeV}$, respectively ⁸.

The cross section $\sigma(\gamma p \rightarrow J/\psi p)$ is measured as a function of Q^2 in the range $0 < Q^2 < 80 \text{ GeV}^2$, and a fit of the form $\sigma_{\gamma p} \propto (M_\psi^2 + Q^2)^{-n}$ yields a value of $n = 2.486 \pm 0.080(\text{stat.}) \pm 0.068(\text{syst.})$. The shape of the Q^2 distribution is well described by a perturbative QCD calculation by Martin, Ryskin and Teubner (MRT), almost independently of the gluon density distribution used.

The photoproduction cross section is measured as a function of the photon-proton centre of mass energy $W_{\gamma p}$ in the range $40 < W_{\gamma p} < 305 \text{ GeV}$, and can be parameterised as $\sigma_{\gamma p} \propto W_{\gamma p}^\delta$ with $\delta = 0.754 \pm 0.033(\text{stat.}) \pm 0.032(\text{syst.})$. The results for δ in electroproduction, measured in the range $40 < W_{\gamma p} < 160 \text{ GeV}$, are consistent with those in photoproduction and no Q^2 dependence is observed within experimental errors. Predictions of the $W_{\gamma p}$ dependence of the cross section in pQCD-based models depend strongly on the gluon distribution, as can be seen explicitly in the MRT model. A good description of the shape of the data can currently be achieved only with some gluon parameterisations. This demonstrates the potential to constrain the gluon distribution with the elastic J/ψ data in a kinematic region (low x , low Q^2) where fits from inclusive data yield gluon distributions with large uncertainties.

The differential cross section $d\sigma/dt$ for elastic J/ψ photoproduction for $|t| \leq 1.2 \text{ GeV}^2$ is measured in the extended range of $40 \leq W_{\gamma p} \leq 305 \text{ GeV}$. A single exponential function yields a good description of $d\sigma/dt$ in this range, while a functional form based on a dipole function is strongly disfavoured. The slope parameter b of the exponential shows a dependence on $W_{\gamma p}$ which is weaker than expected from soft Pomeron phenomenology, but is clearly positive, leading to shrinkage of the diffractive peak. The slope parameter b in electroproduction agrees with the photoproduction values within errors, but has a tendency to decrease with increasing Q^2 .

⁸The results of the present analysis agree within errors with our previous results. We consider the new data to supersede them due to improved statistics and better understanding of the detector efficiencies.

Effective Pomeron trajectories $\alpha_0 + \alpha' t$ for elastic J/ψ photoproduction and electroproduction are determined from a simultaneous analysis of $d\sigma/dt$ as a function of $W_{\gamma p}$ and $|t|$. The electroproduction and photoproduction results are consistent with each other within errors. The trajectory for photoproduction has a t slope which is two standard deviations below the soft Pomeron value but four standard deviations above zero.

Finally, the helicity structure of diffractive J/ψ production is analysed as a function of Q^2 and $|t|$. No evidence is found for a violation of s -channel helicity conservation (SCHC). Assuming SCHC, the ratio of the longitudinal to the transverse polarised photon cross sections is determined as a function of Q^2 and is found to be consistent with QCD calculations.

Acknowledgments

We are grateful to the HERA machine group whose outstanding efforts have made this experiment possible. We thank the engineers and technicians for their work in constructing and maintaining the H1 detector, our funding agencies for financial support, the DESY technical staff for continual assistance and the DESY directorate for support and for the hospitality which they extend to the non DESY members of the collaboration. We thank M. Strikman and T. Teubner for valuable discussions and for making their theoretical predictions available.

References

- [1] S. Aid *et al.* [H1 Collaboration], Nucl. Phys. B **468** (1996) 3 [hep-ex/9602007].
- [2] M. Derrick *et al.* [ZEUS Collaboration], Z. Phys. C **69** (1995) 39 [hep-ex/9507011].
- [3] S. Aid *et al.* [H1 Collaboration], Nucl. Phys. B **472** (1996) 3 [hep-ex/9603005].
- [4] C. Adloff *et al.* [H1 Collaboration], Phys. Lett. B **483** (2000) 23 [hep-ex/0003020].
- [5] J. Breitweg *et al.* [ZEUS Collaboration], Z. Phys. C **75** (1997) 215 [hep-ex/9704013].
- [6] S. Chekanov *et al.* [ZEUS Collaboration], Eur. Phys. J. C **24** (2002) 345 [hep-ex/0201043].
- [7] M. Diehl, Phys. Rept. **388** (2003) 41 [arXiv:hep-ph/0307382].
- [8] L. Frankfurt and M. Strikman, Phys. Rev. D **66** (2002) 031502 [hep-ph/0205223].
- [9] L. Frankfurt, M. McDermott and M. Strikman, JHEP **0103** (2001) 045 [hep-ph/0009086].
- [10] S. J. Brodsky *et al.*, JETP Lett. **70** (1999) 155 [hep-ph/9901229]; N. N. Nikolaev, B. G. Zakharov and V. R. Zoller, Phys. Lett. B **366** (1996) 337 [hep-ph/9506281].
- [11] C. Adloff *et al.* [H1 Collaboration], Eur. Phys. J. C **10** (1999) 373 [hep-ex/9903008].
- [12] C. Adloff *et al.* [H1 Collaboration], Phys. Lett. B **541** (2002) 251 [hep-ex/0205107].

- [13] A. Aktas *et al.* [H1 Collaboration], Phys. Lett. B **568** (2003) 205 [hep-ex/0306013].
- [14] S. Chekanov *et al.* [ZEUS Collaboration], Eur. Phys. J. C **26** (2003) 389 [hep-ex/0205081].
- [15] J. Breitweg *et al.* [ZEUS Collaboration], Eur. Phys. J. C **6** (1999) 603 [hep-ex/9808020].
- [16] S. Chekanov *et al.* [ZEUS Collaboration], Nucl. Phys. B **695** (2004) 3 [hep-ex/0404008].
- [17] P. D. B. Collins, *An Introduction to Regge Theory and High Energy Physics*, Cambridge University Press, 1977.
- [18] A. Donnachie and P. V. Landshoff, Phys. Lett. B **348** (1995) 213.
- [19] A. Donnachie and P. V. Landshoff, Phys. Lett. B **437** (1998) 408; Phys. Lett. B **470** (1999) 243; Phys. Lett. B **478** (2000) 146 [hep-ph/9912312]; Phys. Lett. B **518** (2001) 63 [hep-ph/0105088].
- [20] J. Bartels and H. Kowalski, Eur. Phys. J. C **19** (2001) 693 [hep-ph/0010345].
- [21] M. G. Ryskin, Z. Phys. C **57** (1993) 89.
- [22] A. D. Martin and M. G. Ryskin, Phys. Rev. D **57** (1998) 6692 [hep-ph/9711371].
- [23] D. Y. Ivanov, A. Schäfer, L. Szymanowski and G. Krasnikov, Eur. Phys. J. C **34** (2004) 297 [hep-ph/0401131].
- [24] I. P. Ivanov, N. N. Nikolaev and A. A. Savin, “Diffractive vector meson production at HERA: From soft to hard QCD”, DESY-04-243 (2004) [hep-ph/0501034].
- [25] T. Teubner, Proc. Ringberg Workshop “New Trends in HERA Physics 1999”, ed. G. Grindhammer *et al.*, Ringberg Castle, Germany, Lecture Notes in Physics, Vol. 546, page 349, Springer-Verlag (2000) [hep-ph/9910329].
- [26] A. D. Martin, M. G. Ryskin and T. Teubner, Phys. Rev. D **62** (2000) 014022 [hep-ph/9912551].
- [27] A. G. Shuvaev, K. J. Golec-Biernat, A. D. Martin and M. G. Ryskin, Phys. Rev. D **60** (1999) 014015 [hep-ph/9902410].
- [28] T. Teubner, private communication and contribution to the XIIIth International Workshop on Deep Inelastic Scattering (DIS2005), Madison, Wisconsin (in press, ed. W.H. Smith, Volume 792 in the AIP Conference Proceedings series).
- [29] I. Abt *et al.* [H1 Collaboration], Nucl. Instrum. Meth. A **386** (1997) 310 and 348.
- [30] W. Eick *et al.*, Nucl. Instrum. Meth. A **386** (1997) 81.
- [31] T. Nicholls *et al.* [H1 SpaCal Group], Nucl. Instrum. Meth. A **374** (1996) 149.
- [32] R. D. Appuhn *et al.* [H1 SpaCal Group], Nucl. Instrum. Meth. A **386** (1997) 397.
- [33] P. Biddulph *et al.*, Nucl. Instrum. Meth. A **340** (1994) 304.

- [34] J. K. Köhne *et al.*, Nucl. Instrum. Meth. A **389** (1997) 128.
- [35] S. Bentvelsen, J. Engelen and P. Kooijman, Proceedings of the Workshop “Physics at HERA”, vol. 1, eds. W. Buchmüller, G. Ingelman, DESY (1992) 23; C. Hoeger, *ibid.*, page 43.
- [36] F. Jacquet and A. Blondel, in Proc. of the “Study for an *ep* Facility for Europe”, edited by U. Amaldi (1979) 391, DESY-79-048.
- [37] B. List and A. Mastroberardino, Proc. of the Workshop on Monte Carlo Generators for HERA Physics, eds. A.T. Doyle *et al.*, DESY-PROC-1999-02 (1999) 396.
- [38] A. Kwiatkowski, H. Spiesberger and H. J. Möhring, Comput. Phys. Commun. **69** (1992) 155.
- [39] S. P. Baranov, O. Dünger, H. Shooshtari and J. A. Vermaseren, Proceedings of the Workshop “Physics at HERA”, vol. 3, eds. W. Buchmüller, G. Ingelman, DESY (1992) 1478
- [40] T. Carli, A. Courau, S. Kermiche and P. Kessler, Proceedings of the Workshop “Physics at HERA”, vol. 3, eds. W. Buchmüller, G. Ingelman, DESY (1992) 1468
- [41] T. Abe, Comput. Phys. Commun. **136** (2001) 126 [hep-ph/0012029].
- [42] R. Brun *et al.*, CERN-DD/EE/84-1 (1987).
- [43] P. Fleischmann, PhD thesis, Universität Hamburg, DESY-THESIS-2004-013, (available at http://www-h1.desy.de/publications/theses_list.html).
- [44] L. Janauschek, PhD thesis, Ludwig-Maximilians-Universität München, 2005, (available at http://www-h1.desy.de/publications/theses_list.html).
- [45] A. Aktas *et al.* [H1 Collaboration], Phys. Lett. B **598** (2004) 159 [hep-ex/0406029].
- [46] S. Frixione, M. L. Mangano, P. Nason and G. Ridolfi, Phys. Lett. B **319** (1993) 339 [hep-ph/9310350].
- [47] S. Eidelman *et al.* [Particle Data Group], Phys. Lett. B **592** (2004) 1.
- [48] J. Pumplin *et al.*, JHEP **0207** (2002) 012 [hep-ph/0201195].
- [49] A. D. Martin, R. G. Roberts, W. J. Stirling and R. S. Thorne, Eur. Phys. J. C **23** (2002) 73 [hep-ph/0110215].
- [50] C. Adloff *et al.* [H1 Collaboration], Eur. Phys. J. C **21** (2001) 33 [hep-ex/0012053].
- [51] S. Chekanov *et al.* [ZEUS Collaboration], Phys. Rev. D **67** (2003) 012007 [hep-ex/0208023].
- [52] H. L. Lai *et al.*, Phys. Rev. D **55** (1997) 1280 [hep-ph/9606399].
- [53] G. D’Agostini, Nucl. Instrum. Meth. A **362** (1995) 487; preprint DESY-95-242, ROME-1070-1995 [hep-ph/9512295].

- [54] A. Donnachie and P. V. Landshoff, Phys. Lett. B **437** (1998) 408 [hep-ph/9806344].
- [55] K. Schilling and G. Wolf, Nucl. Phys. B **61** (1973) 381.

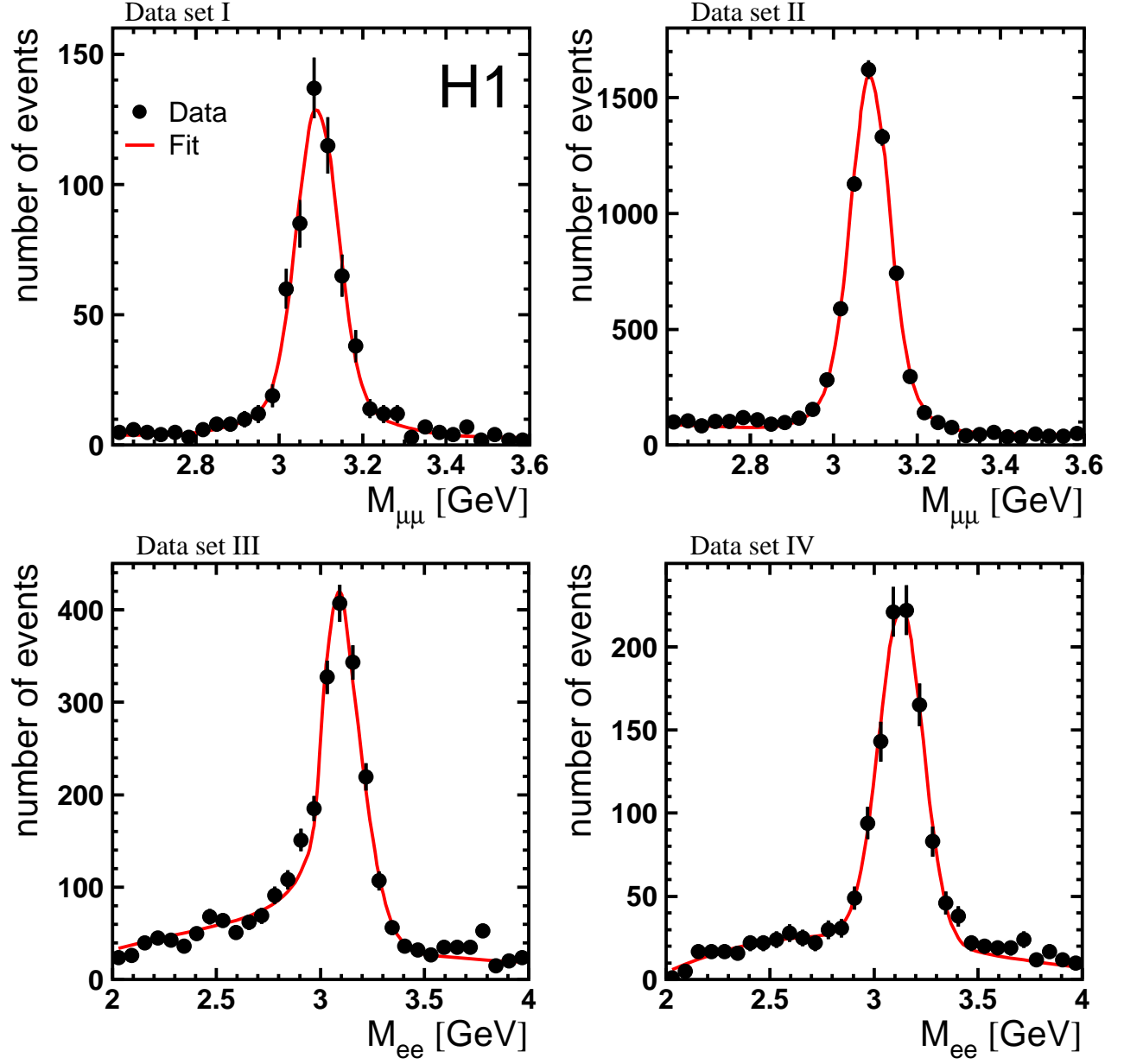


Figure 2: The dilepton invariant mass distributions (data and fits) in the four kinematic regions defined in table 1.

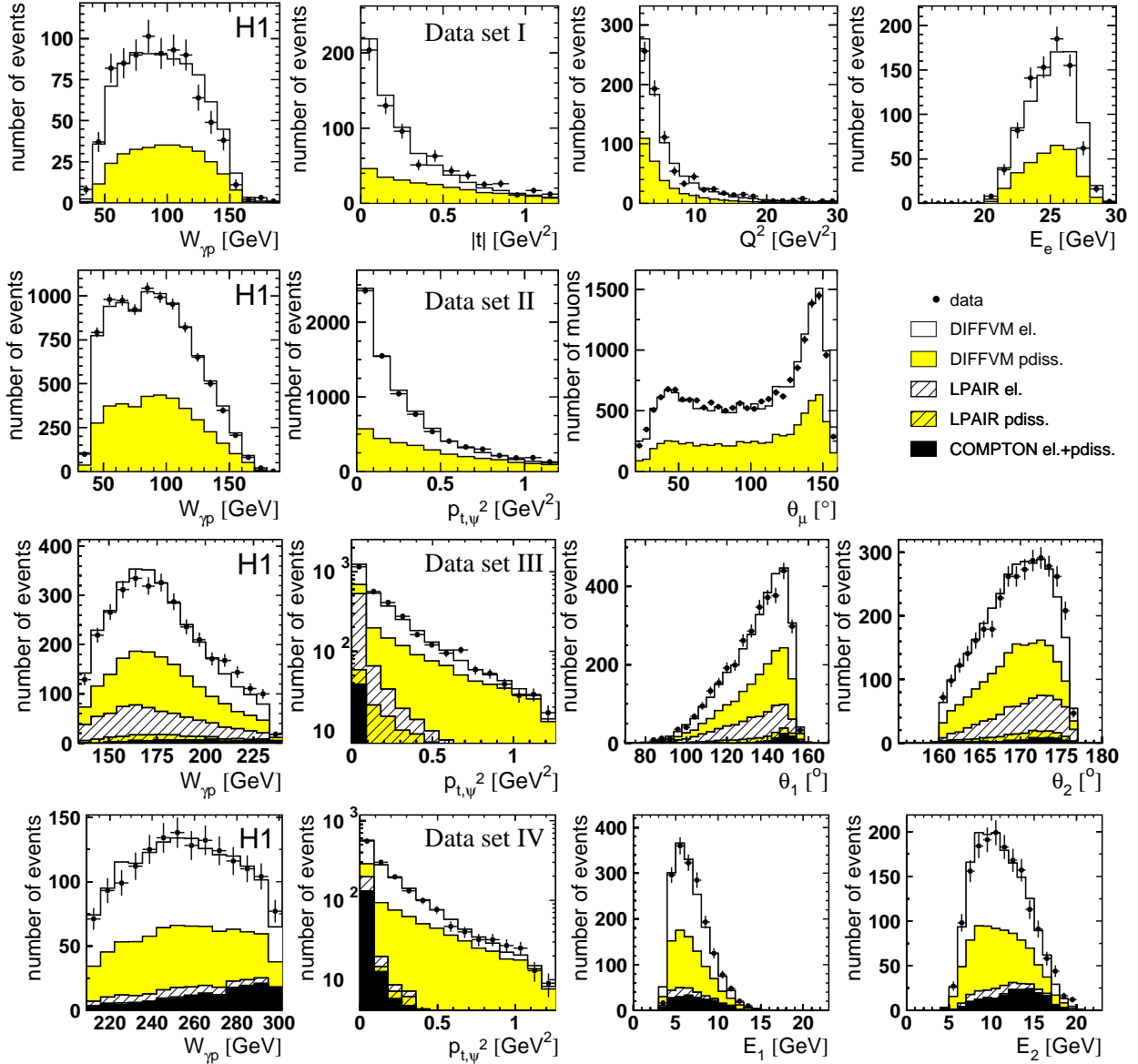


Figure 3: Observed event distributions for the four data sets (points) defined in table 1, omitting the forward detector cuts against proton dissociative events. The first two rows correspond to the selected $J/\psi \rightarrow \mu^+\mu^-$ candidates where the small non-resonant background has been subtracted. The data are shown with the elastic (signal) simulations (DIFFVM el., white area) and proton dissociation MC (DIFFVM pdiss., shaded area). Rows three and four correspond to $J/\psi \rightarrow e^+e^-$ candidates, where the non-resonant background is not subtracted. Here, in addition to the elastic and proton dissociative J/ψ simulations the contributions from $\gamma\gamma \rightarrow e^+e^-$ (LPAIR) and Compton scattering (COMPTON) are shown. The normalisations are obtained from a fit of the overall mass peak of each data set. The variables $W_{\gamma p}$, Q^2 , t and $p_{t,\psi}^2$ are defined in the text. θ_μ refers to the decay muons of data set II. In row three θ_1 and θ_2 refer to the decay electrons which are selected in different polar angular regions. In row four E_1 and E_2 refer to the energies of the decay electrons.

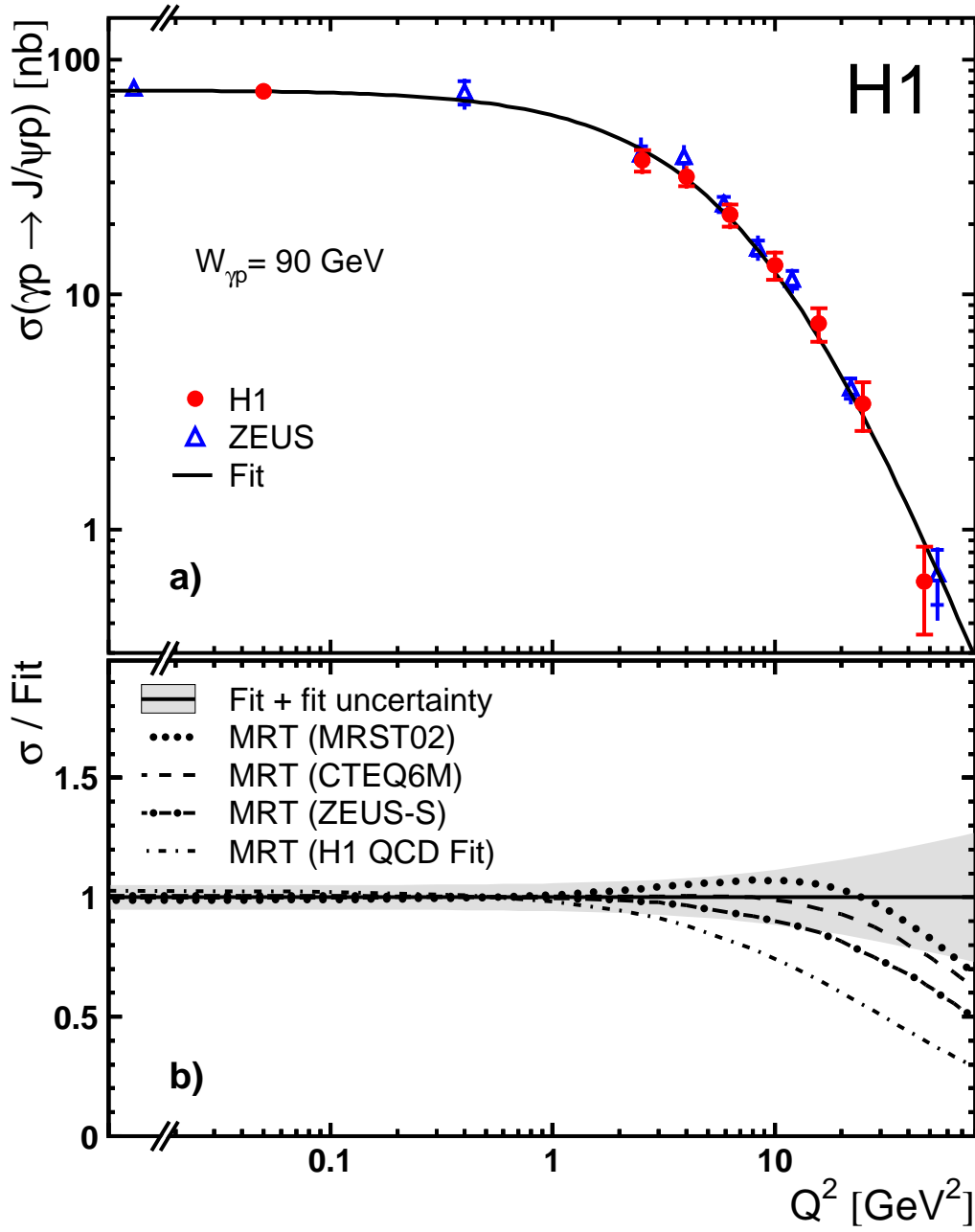


Figure 4: a) Total cross section for elastic J/ψ production as a function of Q^2 in the range $|t| < 1.2 \text{ GeV}^2$ at $W_{\gamma p} = 90 \text{ GeV}$. The inner error bars show the statistical errors, while the outer error bars show the statistical and systematic uncertainties added in quadrature. The solid line is a fit to the H1 data of the form $\sigma_{\gamma p} \propto (M_\psi^2 + Q^2)^{-n}$. Data from the ZEUS experiment [6, 16] are also shown. b) The ratio of the MRT calculations [26] to the fit from a). The MRT QCD predictions are based on different gluon distributions [48–51]. The curves are individually normalised to the measurements across the complete Q^2 range yielding factors between 1.5 and 2.8. The shaded band represents the uncertainty of the fit result.

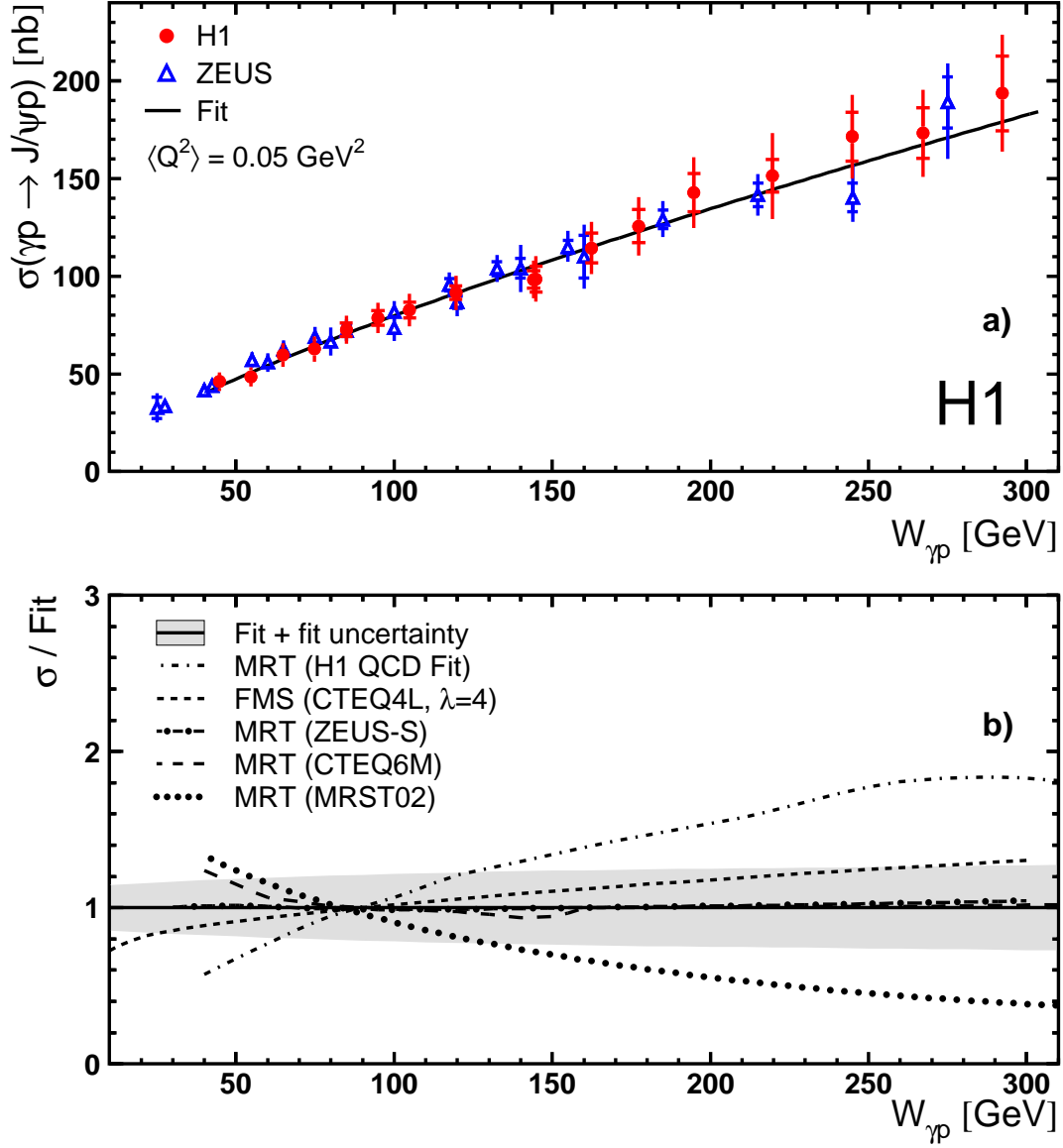


Figure 5: a) Total cross sections for elastic J/ψ production as a function of $W_{\gamma p}$ in the range $|t| < 1.2 \text{ GeV}^2$ in photoproduction. The inner error bars show the statistical errors, while the outer error bars show the statistical and systematic uncertainties added in quadrature. The solid line shows a fit to the H1 data of the form $\sigma \propto W_{\gamma p}^\delta$. Results from the ZEUS experiment [6] in a similar kinematic range are also shown. b) The ratio of theoretical predictions to the fit to the H1 data in a). The shaded band represents the uncertainties of the fit result. Predictions from MRT QCD calculations [26] and a dipole model (FMS, [9]) based on different gluon distributions [48–52] are shown. For the MRT curves the normalisation factors determined from the Q^2 distributions are used. The FMS prediction is normalised to the fit result at $W_{\gamma p} = 90 \text{ GeV}$.

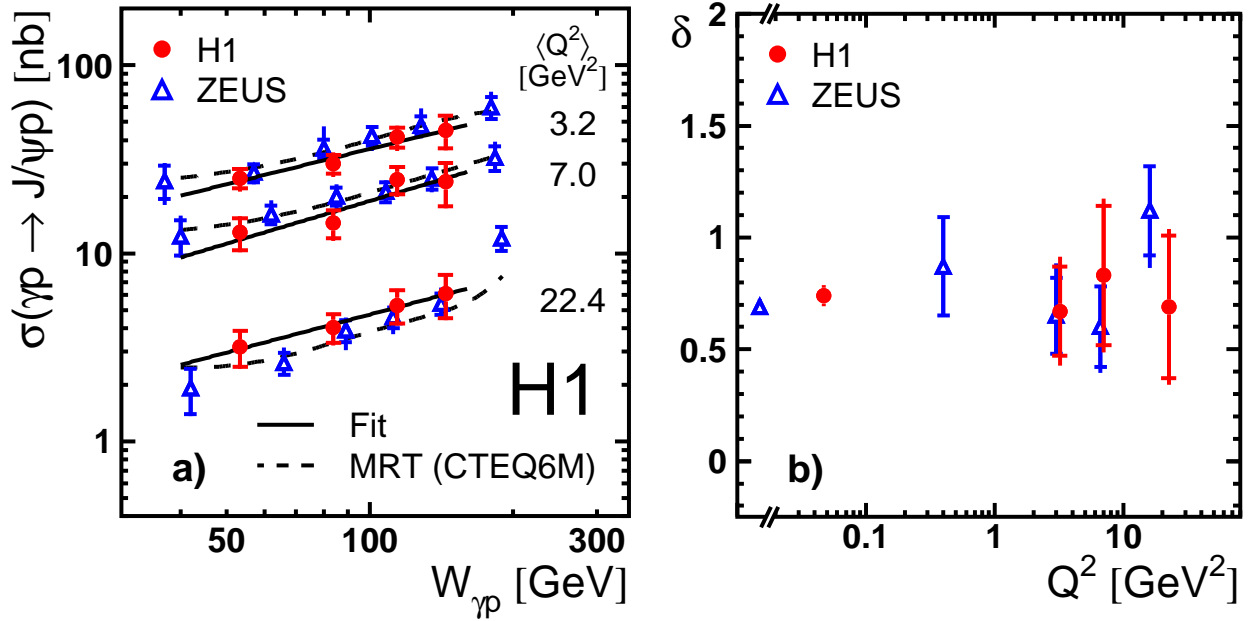


Figure 6: a) Total cross sections for elastic J/ψ production as a function of $W_{\gamma p}$ in the range $|t| < 1.2 \text{ GeV}^2$ in electroproduction in three bins of Q^2 . $\langle Q^2 \rangle$ indicates the bin centre value in the Q^2 range considered. The solid lines show fits to the H1 data of the form $\sigma \propto W_{\gamma p}^\delta$. The dashed curves show the MRT QCD prediction based on the gluon distribution CTEQ6M [48] with the normalisation factors from the fit to the Q^2 distribution. Results from the ZEUS experiment [16] in a similar kinematic range are also shown. They have been scaled to the given $\langle Q^2 \rangle$ values using the Q^2 dependence measured by ZEUS. b) The fit parameter δ as a function of Q^2 . The inner error bars show the statistical error, while the outer error bars show the statistical and systematic uncertainties added in quadrature.

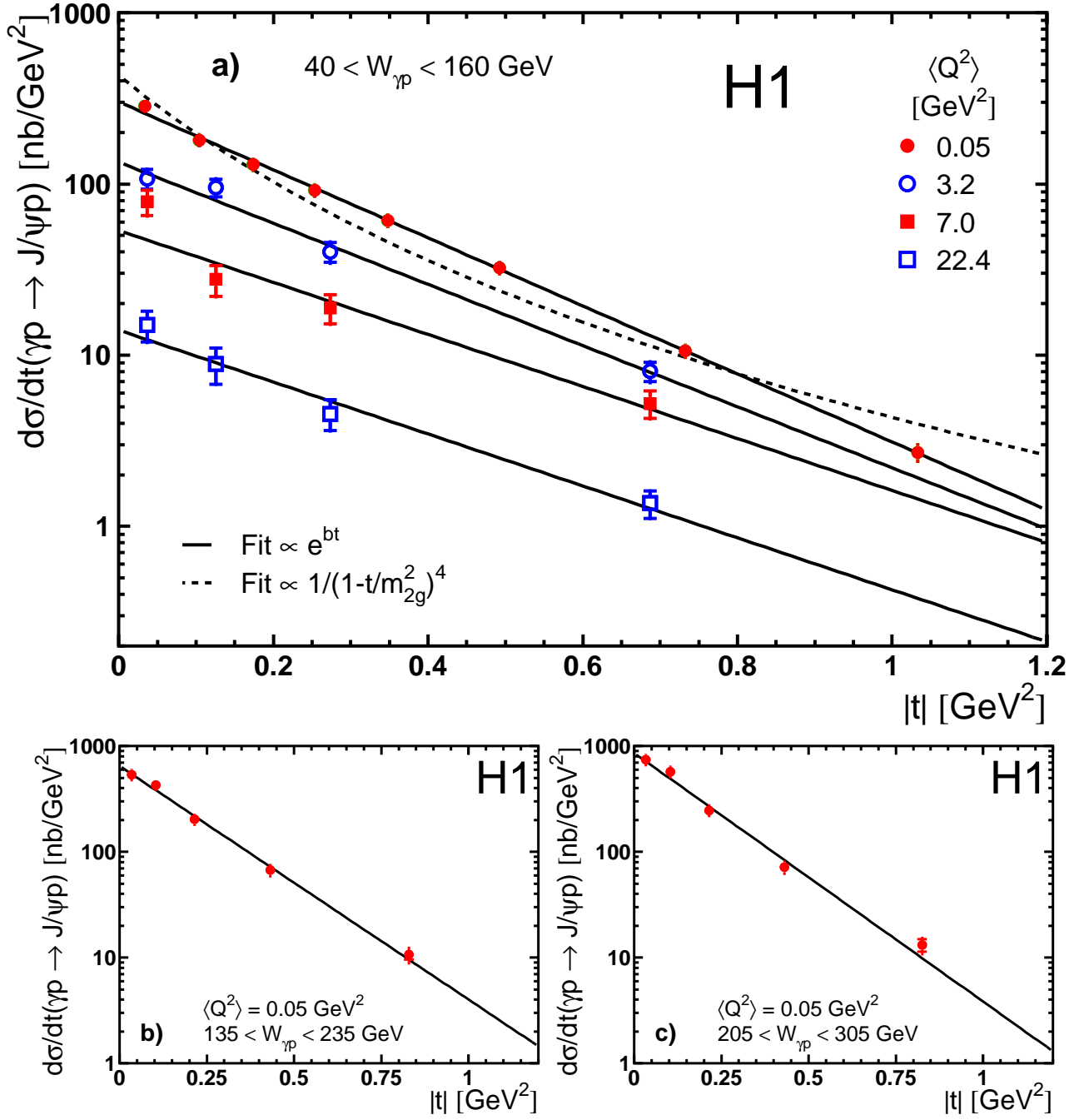


Figure 7: Differential cross section $d\sigma/dt$ for elastic J/ψ production as a function of $|t|$ a) in four bins of Q^2 in the range $40 < W_{\gamma p} < 160$ GeV. $\langle Q^2 \rangle$ indicates the bin centre value in the Q^2 range considered. The inner error bars show the statistical error, while the outer error bars show the statistical and systematic uncertainties added in quadrature. The solid lines show fits to the data of the form $d\sigma/dt \propto e^{bt}$. The dashed curve shows the result of a fit proposed by Frankfurt and Strikman [8]. Figures b) and c) show the photoproduction measurements in the ranges $135 < W_{\gamma p} < 235$ GeV and $205 < W_{\gamma p} < 305$ GeV.

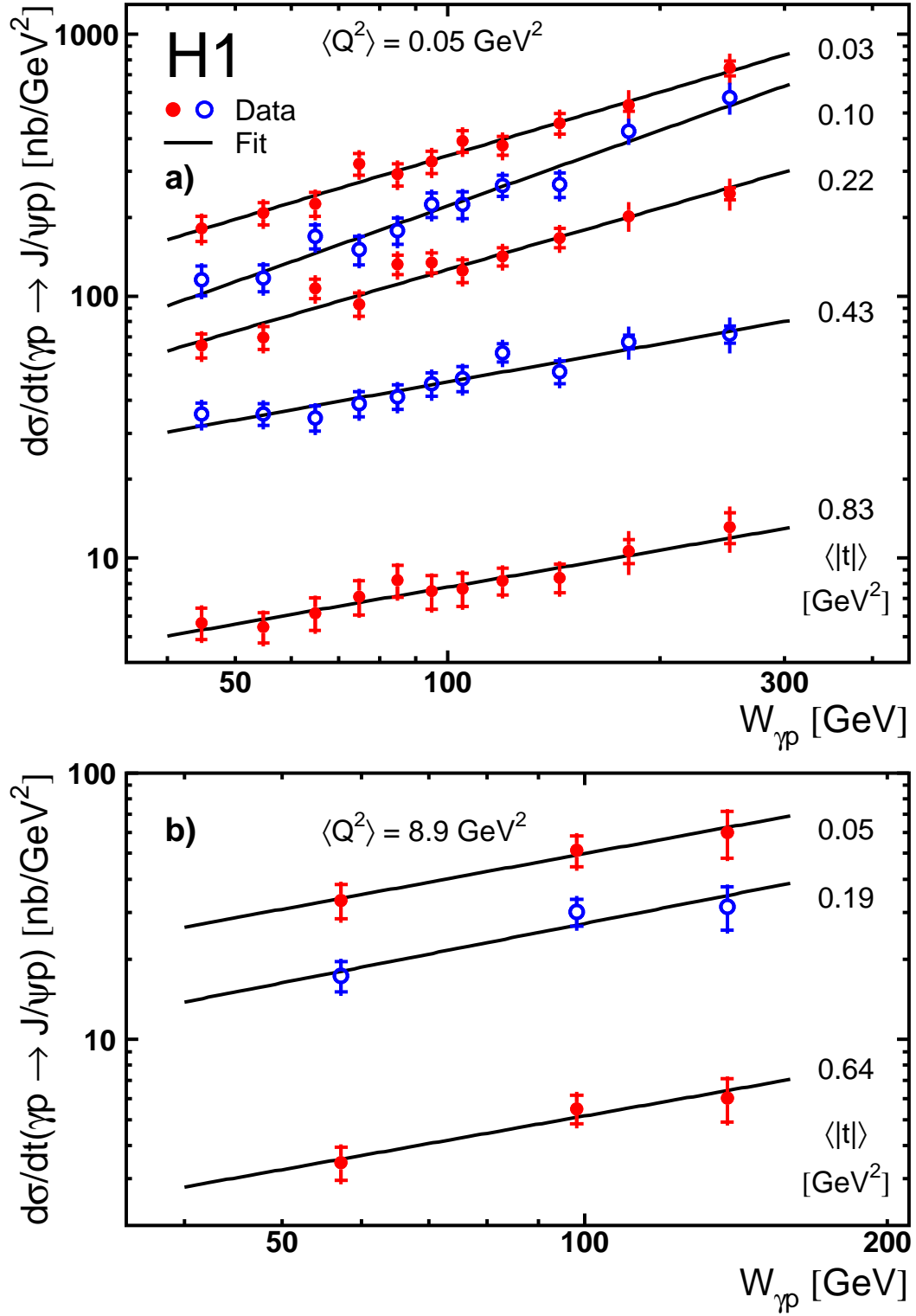


Figure 8: Differential cross section $d\sigma/dt$ for elastic J/ψ production as a function of $W_{\gamma p}$ in bins of $|t|$ a) in photoproduction and b) in electroproduction. $\langle Q^2 \rangle$ and $\langle |t| \rangle$ indicate the bin centre values in the ranges considered. The inner error bars show the statistical error, while the outer error bars show the statistical and systematic uncertainties added in quadrature. The solid lines show the results of one-dimensional fits of the form $\sigma \propto W_{\gamma p}^{4(\alpha(\langle t \rangle)-1)}$ in each t bin.

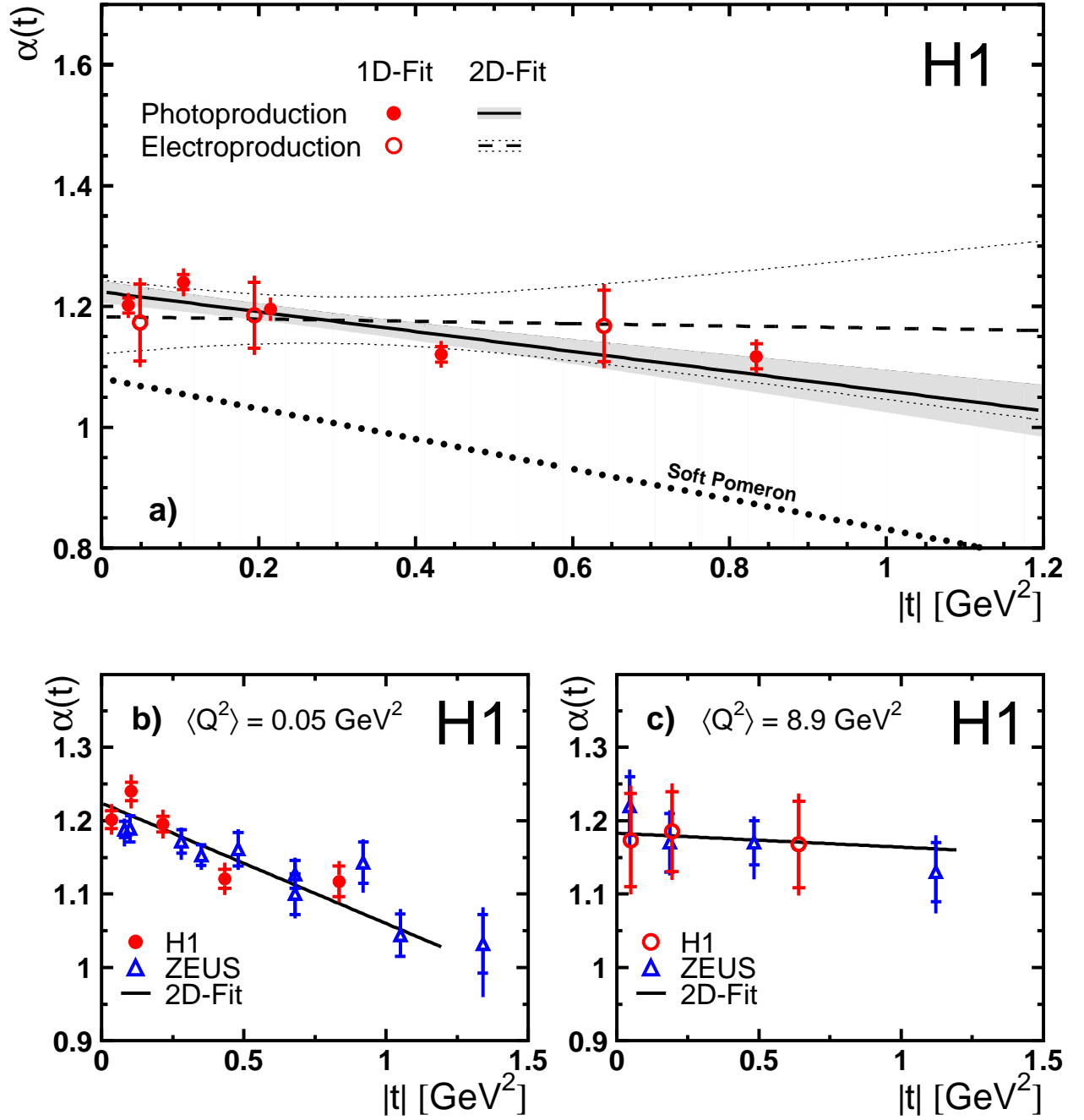


Figure 9: a) The effective trajectory $\alpha(t)$ as a function of $|t|$ in the range $40 < W_{\gamma p} < 305 \text{ GeV}$ for photoproduction ($\langle Q^2 \rangle = 0.05 \text{ GeV}^2$) and $40 < W_{\gamma p} < 160 \text{ GeV}$ for electroproduction ($\langle Q^2 \rangle = 8.9 \text{ GeV}^2$). The data points are the results of the one-dimensional fits shown in figure 8. The inner error bars show the statistical error, while the outer error bars show the statistical and systematic uncertainties added in quadrature. The solid and dashed lines show the results of two-dimensional fits (equation 2) together with 1σ -error bands, which take the correlation between the fit parameters into account. A comparison with the results of the ZEUS collaboration [6, 16] is shown in b) and c) for photoproduction and electroproduction respectively. The data in [16] are derived at slightly different values of $\langle Q^2 \rangle$. The lines are results from the two-dimensional fits.

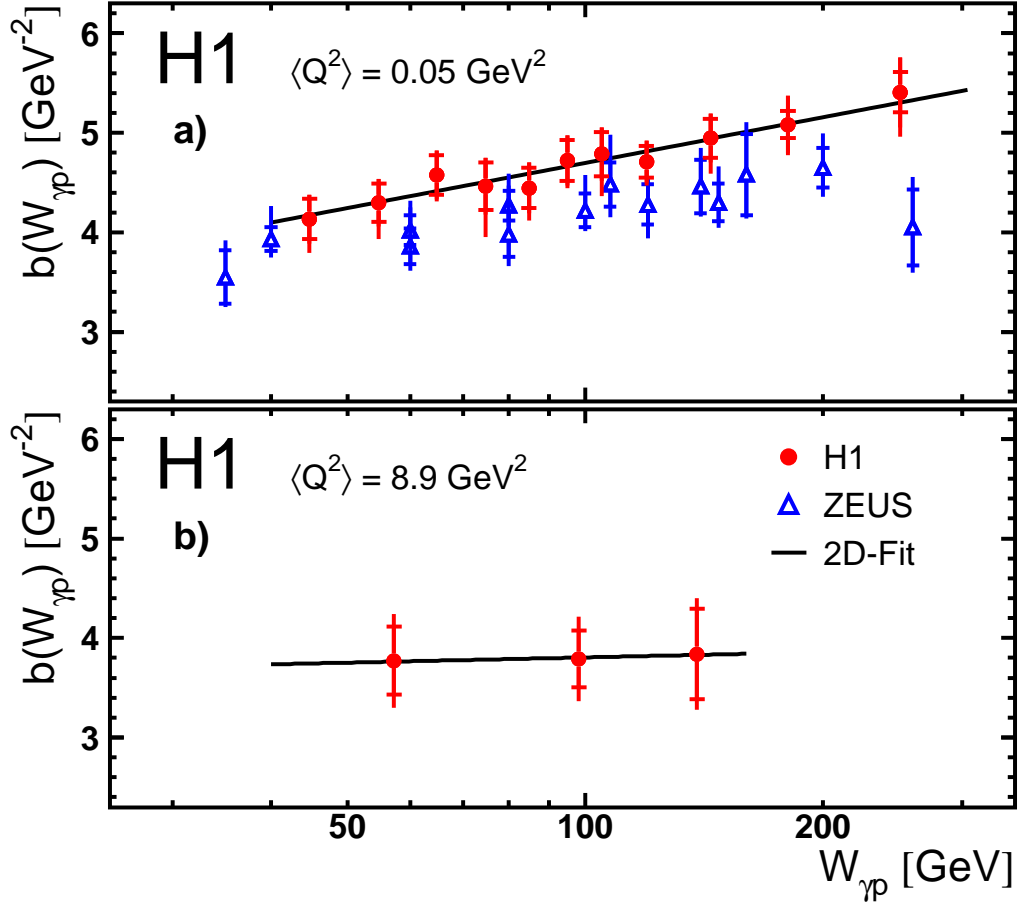


Figure 10: The values of the t slope parameter $b(W_{\gamma p})$ as a function of $W_{\gamma p}$ in the range $|t| < 1.2 \text{ GeV}^2$ for a) photoproduction and b) electroproduction. $\langle Q^2 \rangle$ indicates the bin centre value in the Q^2 range considered. The data points are the results of one-dimensional fits of the form $d\sigma/dt \propto e^{bt}$ in $W_{\gamma p}$ bins. The inner error bars show the statistical errors, while the outer error bars show the statistical and systematic uncertainties added in quadrature. The solid lines show the results of the two-dimensional fits (equation 2) as in figure 9. In a) the data are compared with results from the ZEUS collaboration [6].

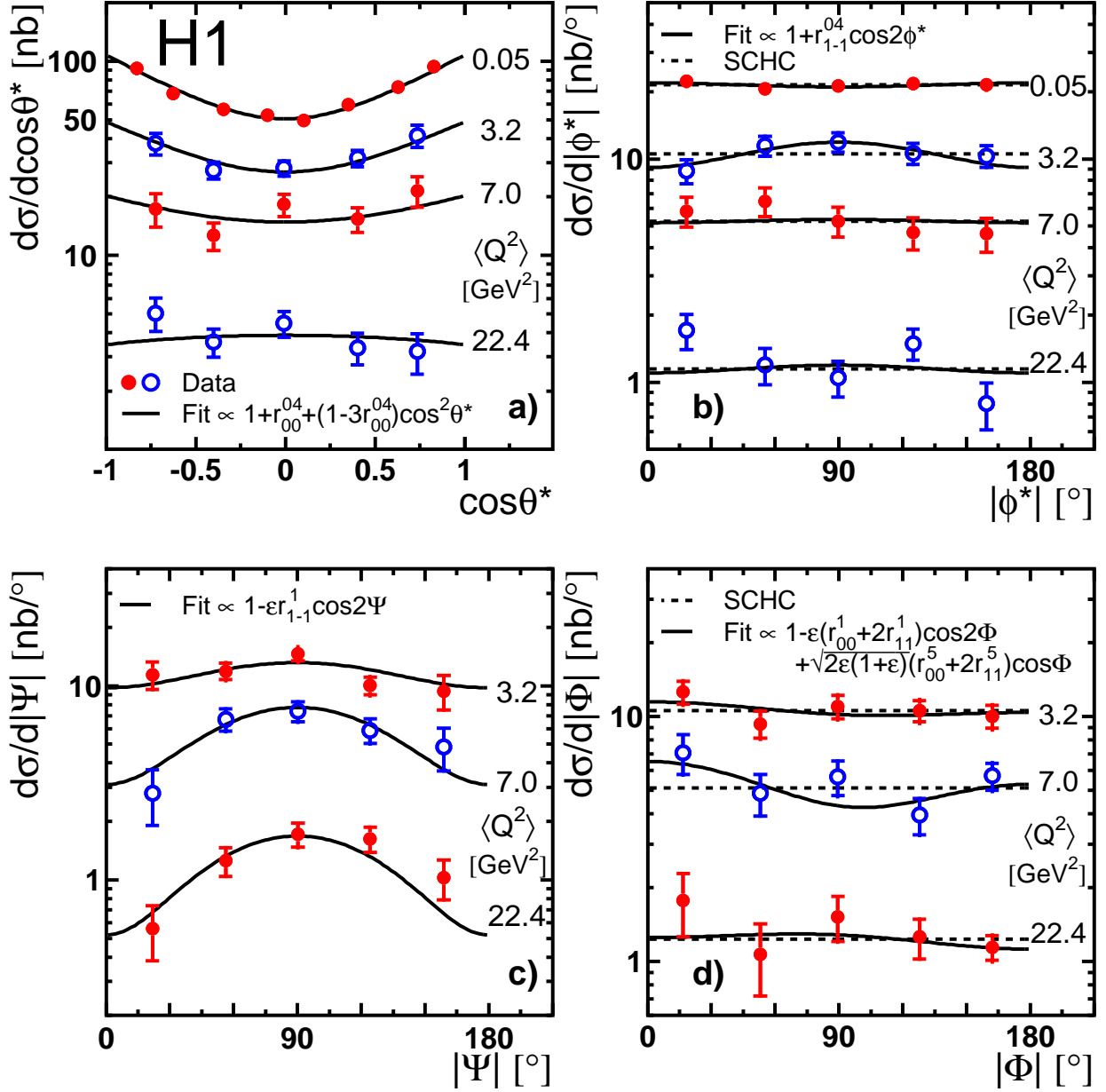


Figure 11: The differential cross sections for diffractive (elastic and proton dissociative) J/ψ production as functions of the four angles θ^* , ϕ^* , Ψ and Φ defined in the text. The data are shown in bins of Q^2 for the range $40 < W_{\gamma p} < 160$ GeV and $|t| < 5$ GeV². $\langle Q^2 \rangle$ indicates the bin centre value in the Q^2 range considered. The inner error bars show the statistical error, while the outer error bars show the statistical and systematic uncertainties added in quadrature. The solid lines represent the results of fits to the data. The dashed lines in b) and d) are fits assuming s -channel helicity conservation.

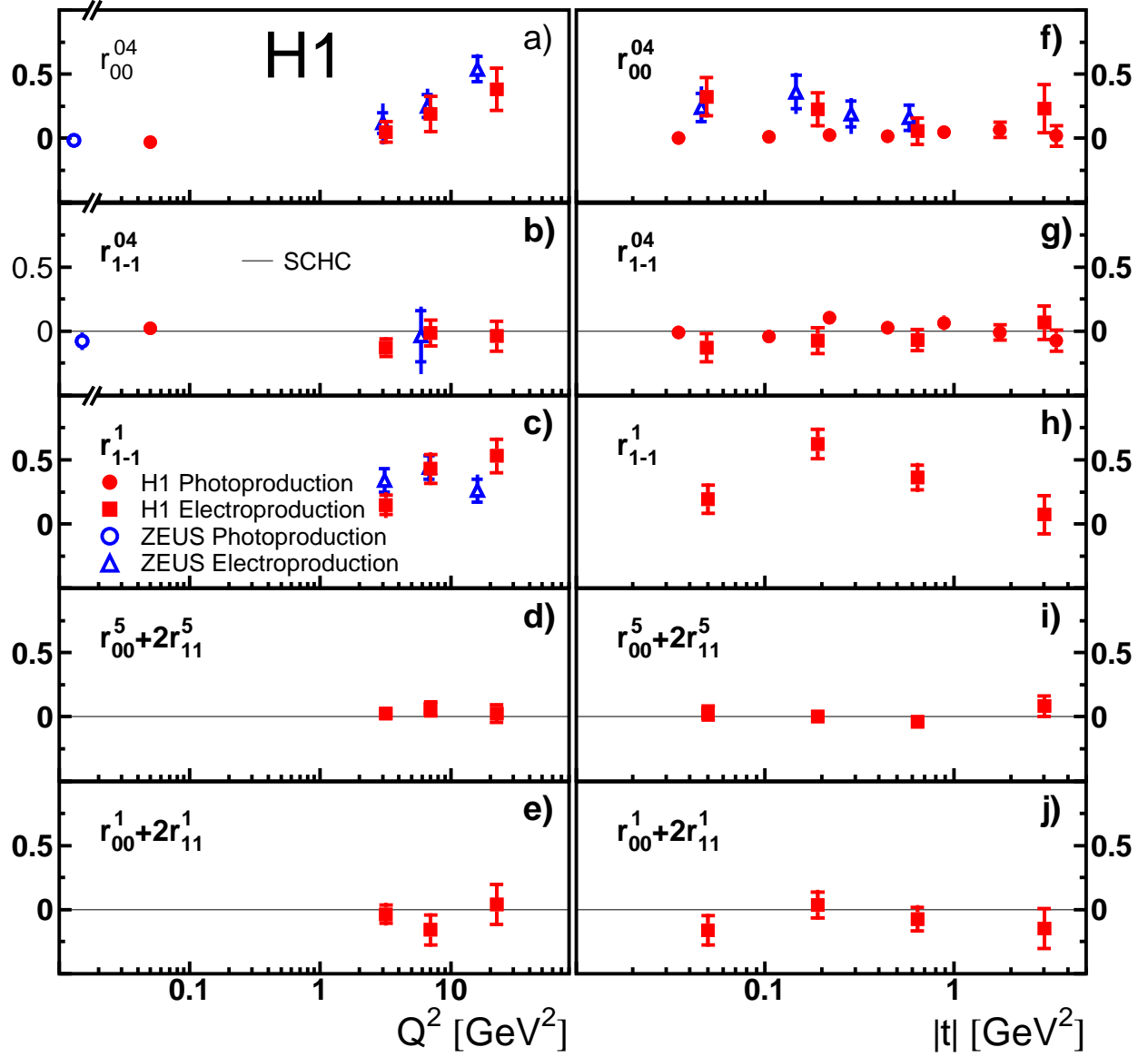


Figure 12: Spin-density matrix elements as functions of Q^2 (a-e) and $|t|$ (f-j) for the range $40 < W_{\gamma p} < 160$ GeV. The data points are the results of fits of equations 4- 7 to the data shown in figure 11. The inner error bars show the fit result including only the statistical error, while the outer error bars also include the systematic uncertainties. The expectations from SCHC are shown as solid lines. The results from the ZEUS collaboration are also shown, (a), c) and f) [6, 16] and b) [5, 15]).

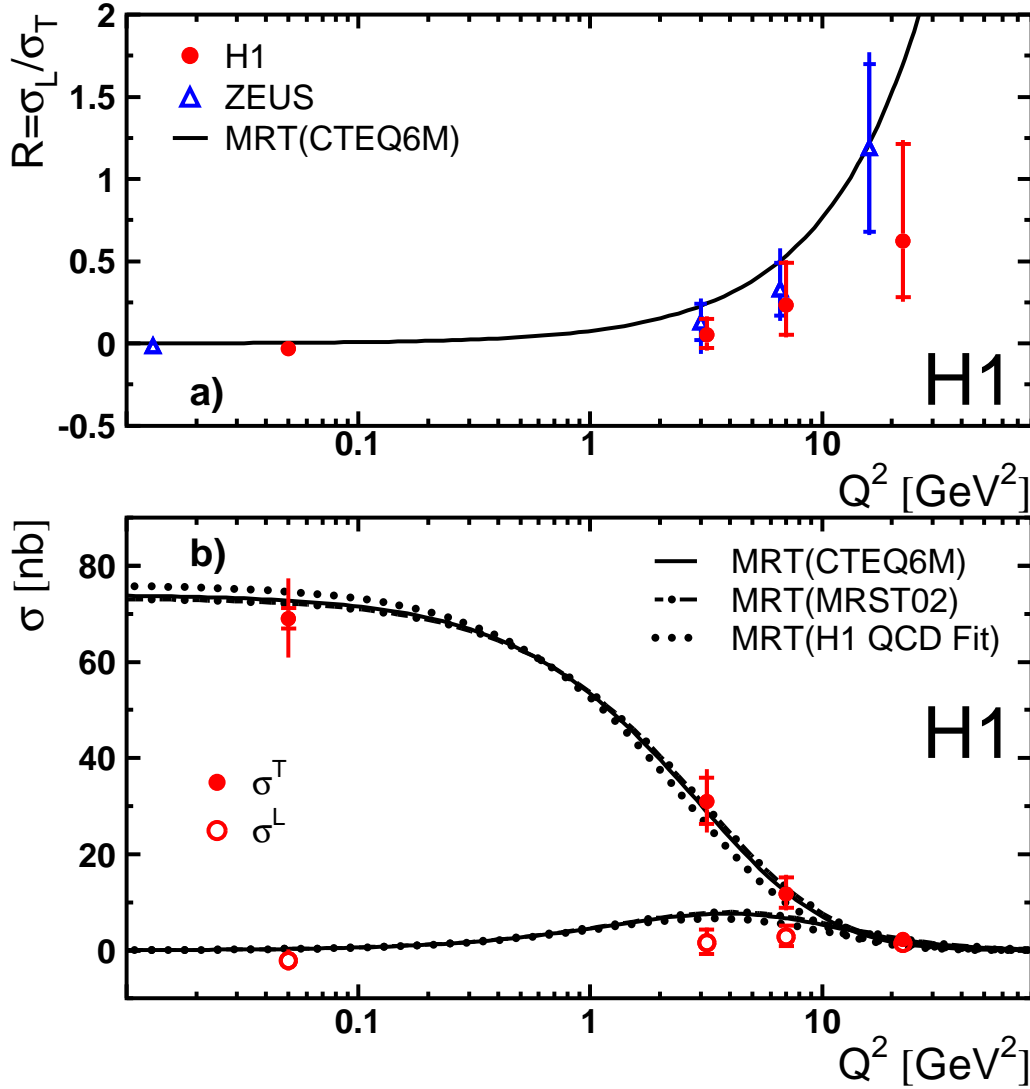


Figure 13: a) Ratio $R = \sigma^L/\sigma^T$ as a function of Q^2 for the range $40 < W_{\gamma p} < 160$ GeV and $|t| < 5$ GeV². The data are compared with the result of a MRT calculation [26] based on the CTEQ6M [48] gluon distribution. Also shown are results from the ZEUS collaboration [6, 16]. b) The cross sections for longitudinally and transversely polarised photons σ^L and σ^T as a function of Q^2 . The MRT QCD calculations based on different gluon distributions ([48–50]) are also shown with the same normalisation factors as derived from figure 4. The inner error bars show the statistical errors, while the outer error bars show the total errors.

Q^2 [GeV ²]	$\langle Q^2 \rangle$ [GeV ²]	σ [nb]
$\lesssim 1$	0.05	$73.1 \pm 1.1 \pm 6.4$
2 – 3.2	2.5	$37.3 \pm 3.9 \pm 3.6$
3.2 – 5.0	4.0	$31.7 \pm 2.7 \pm 3.0$
5.0 – 8.0	6.3	$21.8 \pm 2.4 \pm 2.1$
8.0 – 12.7	10.0	$13.3 \pm 1.8 \pm 1.3$
12.7 – 20.1	15.8	$7.53 \pm 1.24 \pm 0.72$
20.1 – 31.8	25.0	$3.43 \pm 0.81 \pm 0.33$
31.8 – 80.0	47.3	$0.60 \pm 0.24 \pm 0.06$

Table 2: Cross section for the elastic process $\gamma p \rightarrow J/\psi p$ measured in bins of Q^2 for $W_{\gamma p} = 90$ GeV and for $|t| < 1.2$ GeV². $\langle Q^2 \rangle$ indicates the bin centre value in the Q^2 range considered. The first error is statistical and the second the total systematic uncertainty.

Data set	$W_{\gamma p}$ [GeV]	$\langle W_{\gamma p} \rangle$ [GeV]	σ [nb]
II	40 – 50	44.8	$46.0 \pm 2.4 \pm 4.0$
	50 – 60	54.8	$48.5 \pm 2.3 \pm 4.3$
	60 – 70	64.8	$59.7 \pm 2.8 \pm 5.3$
	70 – 80	74.8	$62.7 \pm 3.2 \pm 5.5$
	80 – 90	84.9	$72.6 \pm 3.4 \pm 6.4$
	90 – 100	94.9	$78.6 \pm 3.7 \pm 6.9$
	100 – 110	104.9	$82.6 \pm 4.0 \pm 7.3$
	110 – 130	119.5	$91.5 \pm 3.5 \pm 8.1$
III	130 – 160	144.1	$98.3 \pm 4.4 \pm 8.7$
	135 – 155	144.9	$98.6 \pm 6.6 \pm 9.6$
	155 – 170	162.5	$114 \pm 8 \pm 11$
	170 – 185	177.3	$126 \pm 8 \pm 12$
	185 – 205	194.8	$143 \pm 10 \pm 15$
IV	205 – 235	219.6	$187 \pm 14 \pm 25$
	205 – 235	219.6	$133 \pm 10 \pm 18$
	235 – 255	244.8	$171 \pm 13 \pm 17$
	255 – 280	267.2	$173 \pm 13 \pm 18$
	280 – 305	292.3	$194 \pm 19 \pm 23$

Table 3: Photoproduction cross section for the elastic process $\gamma p \rightarrow J/\psi p$ in bins of $W_{\gamma p}$ for $|t| < 1.2$ GeV² using the data sets II-IV (table 1). $\langle W_{\gamma p} \rangle$ indicates the bin centre value in the $W_{\gamma p}$ range considered. The first error on the cross section is statistical and the second the total systematic uncertainty. Note that there is an overlapping bin between data sets III and IV at $\langle W_{\gamma p} \rangle = 219.6$ GeV, which is averaged for figure 5 to $\sigma = 151 \pm 8 \pm 20$ nb.

Q^2 [GeV ²]	$\langle Q^2 \rangle$ [GeV ²]	$W_{\gamma p}$ [GeV]	$\langle W_{\gamma p} \rangle$ [GeV]	σ [nb]
2 – 5	3.2	40 – 70	53.3	$25.1 \pm 2.9 \pm 2.4$
		70 – 100	83.9	$30.0 \pm 3.4 \pm 2.9$
		100 – 130	114.1	$41.5 \pm 5.1 \pm 4.0$
		130 – 160	144.2	$45.0 \pm 8.8 \pm 4.5$
5 – 10	7.0	40 – 70	53.3	$12.9 \pm 2.5 \pm 1.2$
		70 – 100	83.9	$14.5 \pm 2.5 \pm 1.4$
		100 – 130	114.1	$24.7 \pm 4.1 \pm 2.4$
		130 – 160	144.2	$24.1 \pm 6.2 \pm 2.5$
10 – 80	22.4	40 – 70	53.4	$3.19 \pm 0.69 \pm 0.31$
		70 – 100	83.9	$4.04 \pm 0.70 \pm 0.39$
		100 – 130	114.1	$5.29 \pm 1.0 \pm 0.5$
		130 – 160	144.2	$6.10 \pm 1.6 \pm 0.6$

Table 4: Total cross section for the elastic process $\gamma p \rightarrow J/\psi p$ measured in bins of Q^2 and $W_{\gamma p}$ for $|t| < 1.2 \text{ GeV}^2$. $\langle Q^2 \rangle$ and $\langle W_{\gamma p} \rangle$ are the bin centre values in the indicated ranges. The first error on the cross section is statistical and the second the total systematic uncertainty.

Q^2 [GeV ²]	$\langle Q^2 \rangle$ [GeV ²]	δ	b [GeV ⁻²]
$\lesssim 1$	0.05	$0.75 \pm 0.03 \pm 0.03$	$4.57 \pm 0.06^{+0.11}_{-0.18}$
2 – 5	3.2	$0.67 \pm 0.20 \pm 0.14$	$4.11 \pm 0.26 \pm 0.37$
5 – 10	7.0	$0.83 \pm 0.31 \pm 0.15$	$3.50 \pm 0.50 \pm 0.49$
10 – 80	22.4	$0.69 \pm 0.32 \pm 0.14$	$3.49 \pm 0.45 \pm 0.33$

Table 5: The parameters δ ($\sigma \propto W_{\gamma p}^\delta$) and b ($\frac{d\sigma}{dt} \propto e^{bt}$) measured in bins of Q^2 in the range $40 < W_{\gamma p} < 160 \text{ GeV}$ and $|t| < 1.2 \text{ GeV}^2$. The values $\langle Q^2 \rangle$ indicate the bin centre value in the Q^2 range considered. The first error is statistical and the second systematic.

Q^2 [GeV ²]	$\langle Q^2 \rangle$ [GeV ²]	$ t $ [GeV ²]	$\langle t \rangle$ [GeV ²]	$d\sigma/dt$ [nb/GeV ²]
$\lesssim 1$	0.05	0 – 0.07	0.03	$285 \pm 9 \pm 25$
		0.07 – 0.14	0.10	$180 \pm 7 \pm 16$
		0.14 – 0.21	0.17	$130 \pm 6 \pm 11$
		0.21 – 0.30	0.25	$92.1 \pm 4.0 \pm 8.1$
		0.30 – 0.40	0.35	$61.2 \pm 3.1 \pm 5.4$
		0.40 – 0.60	0.49	$32.5 \pm 1.5 \pm 2.9$
		0.60 – 0.90	0.73	$10.60 \pm 0.60 \pm 0.90$
		0.90 – 1.20	1.03	$2.70 \pm 0.20 \pm 0.30$
2 – 5	3.2	0 – 0.08	0.04	$107 \pm 14 \pm 10$
		0.08 – 0.18	0.13	$95.1 \pm 11.0 \pm 9.1$
		0.18 – 0.38	0.27	$40.2 \pm 5.4 \pm 3.9$
		0.38 – 1.20	0.68	$8.04 \pm 1.05 \pm 0.77$
5 – 10	7.0	0 – 0.08	0.04	$78.6 \pm 13.2 \pm 7.5$
		0.08 – 0.18	0.13	$27.7 \pm 5.7 \pm 2.7$
		0.18 – 0.38	0.27	$18.9 \pm 3.7 \pm 1.8$
		0.38 – 1.20	0.68	$5.21 \pm 0.96 \pm 0.50$
10 – 80	22.4	0 – 0.08	0.04	$15.0 \pm 3.1 \pm 1.4$
		0.08 – 0.18	0.13	$8.90 \pm 2.14 \pm 0.85$
		0.18 – 0.38	0.27	$4.55 \pm 0.93 \pm 0.44$
		0.38 – 1.20	0.68	$1.36 \pm 0.25 \pm 0.13$

Table 6: Differential cross section for the elastic process $\gamma p \rightarrow J/\psi p$ measured in bins of Q^2 and $|t|$ in the range $40 < W_{\gamma p} < 160$ GeV using the data sets I and II (table 1). $\langle Q^2 \rangle$ and $\langle |t| \rangle$ are the bin centre values in the indicated ranges. The first error on the cross section is statistical and the second is the total systematic uncertainty.

	$d\sigma/dt$ [nb/ GeV ²]					
$\langle W_{\gamma p} \rangle$ [GeV]	$ t $ [GeV ²]	0 – 0.07	0.07 – 0.14	0.14 – 0.30	0.30 – 0.60	0.60 – 1.20
45		$182 \pm 20 \pm 16$	$115 \pm 15 \pm 10$	$64.9 \pm 6.7 \pm 5.7$	$35.5 \pm 3.6 \pm 3.1$	$5.7 \pm 0.8 \pm 0.5$
55		$208 \pm 20 \pm 18$	$118 \pm 14 \pm 10$	$69.6 \pm 6.9 \pm 6.1$	$35.6 \pm 3.4 \pm 3.1$	$5.5 \pm 0.7 \pm 0.5$
65		$225 \pm 23 \pm 20$	$169 \pm 18 \pm 15$	$107.1 \pm 9.4 \pm 9.4$	$34.3 \pm 3.7 \pm 3.0$	$6.2 \pm 0.9 \pm 0.5$
75		$321 \pm 31 \pm 28$	$151 \pm 19 \pm 13$	$93.4 \pm 9.5 \pm 8.2$	$38.9 \pm 4.3 \pm 3.4$	$7.1 \pm 1.1 \pm 0.6$
85		$292 \pm 29 \pm 26$	$178 \pm 20 \pm 16$	$132 \pm 11 \pm 12$	$41.4 \pm 4.4 \pm 3.6$	$8.2 \pm 1.1 \pm 0.7$
95		$326 \pm 32 \pm 29$	$224 \pm 24 \pm 20$	$135 \pm 12 \pm 12$	$46.3 \pm 4.8 \pm 4.1$	$7.5 \pm 1.1 \pm 0.7$
105		$392 \pm 37 \pm 34$	$224 \pm 26 \pm 20$	$125 \pm 12 \pm 11$	$48.5 \pm 5.3 \pm 4.3$	$7.7 \pm 1.1 \pm 0.7$
119		$376 \pm 31 \pm 33$	$265 \pm 24 \pm 23$	$142 \pm 11 \pm 12$	$60.9 \pm 4.9 \pm 5.4$	$8.2 \pm 1.0 \pm 0.7$
144		$458 \pm 42 \pm 40$	$267 \pm 29 \pm 23$	$167 \pm 14 \pm 15$	$51.5 \pm 5.3 \pm 4.5$	$8.4 \pm 1.1 \pm 0.7$
181		$537 \pm 28 \pm 68$	$427 \pm 18 \pm 46$	$202 \pm 9 \pm 25$	$67.0 \pm 4.1 \pm 8.8$	$10.7 \pm 1.1 \pm 1.7$
251		$744 \pm 48 \pm 88$	$573 \pm 28 \pm 75$	$246 \pm 13 \pm 32$	$71.6 \pm 5.5 \pm 9.8$	$13.1 \pm 1.8 \pm 1.9$

Table 7: Differential photoproduction cross sections $d\sigma/dt$ for the elastic process $\gamma p \rightarrow J/\psi p$ measured in bins of $W_{\gamma p}$ and $|t|$ using data sets II-IV (table 1). The first error is statistical and the second the total systematic uncertainty.

	$d\sigma/dt$ [nb/ GeV ²]			
$\langle W_{\gamma p} \rangle$ [GeV]	$ t $ [GeV ²]	0 – 0.1	0.1 – 0.3	0.3 – 1.2
57		$33.3 \pm 4.9 \pm 3.2$	$17.3 \pm 2.2 \pm 1.7$	$3.4 \pm 0.5 \pm 0.3$
98		$51.3 \pm 6.7 \pm 4.9$	$30.1 \pm 3.5 \pm 2.9$	$5.5 \pm 0.7 \pm 0.5$
140		$60 \pm 12 \pm 6$	$31.5 \pm 5.8 \pm 3.0$	$6.0 \pm 1.1 \pm 0.6$

Table 8: Differential electroproduction ($\langle Q^2 \rangle = 8.9$ GeV²) cross section $d\sigma/dt$ for the elastic process $\gamma p \rightarrow J/\psi p$ measured in bins of $W_{\gamma p}$ and $|t|$ using data set I (table 1). The first error is statistical and the second the total systematic uncertainty.

$\langle Q^2 \rangle$ [GeV ²]	$ t $ [GeV ²]	$\langle t \rangle$ [GeV ²]	$\alpha(\langle t \rangle)$
0.05	0 – 0.07	0.03	$1.202 \pm 0.012 \pm 0.017$
	0.07 – 0.14	0.10	$1.240 \pm 0.012 \pm 0.019$
	0.14 – 0.30	0.22	$1.195 \pm 0.011 \pm 0.016$
	0.30 – 0.60	0.43	$1.121 \pm 0.013 \pm 0.018$
	0.60 – 1.20	0.84	$1.117 \pm 0.021 \pm 0.019$
8.9	0 – 0.1	0.05	$1.173 \pm 0.064 \pm 0.038$
	0.1 – 0.3	0.19	$1.185 \pm 0.054 \pm 0.037$
	0.3 – 1.2	0.64	$1.168 \pm 0.059 \pm 0.037$

Table 9: The effective Pomeron trajectories $\alpha(t)$ derived from one-dimensional fits of the $W_{\gamma p}$ dependence in bins of t , in the ranges $Q^2 \lesssim 1$ GeV², $40 < W_{\gamma p} < 305$ GeV (photoproduction) and $2 < Q^2 < 80$ GeV², $40 < W_{\gamma p} < 160$ GeV (electroproduction). The values $\langle Q^2 \rangle$ and $\langle |t| \rangle$ are the bin centre values in the indicated ranges. The first error is statistical and the second systematic.

Data set	$\langle Q^2 \rangle$ [GeV ²]	$W_{\gamma p}$ [GeV]	$\langle W_{\gamma p} \rangle$ [GeV]	$b(\langle W_{\gamma p} \rangle)$ [GeV ⁻²]
I	8.9	40 – 80	57.3	$3.77 \pm 0.34 \pm 0.33$
		80 – 120	98.2	$3.79 \pm 0.29 \pm 0.32$
		120 – 160	139.6	$3.84 \pm 0.45 \pm 0.33$
II	0.05	40 – 50	44.8	$4.13 \pm 0.20^{+0.14}_{-0.27}$
		50 – 60	54.8	$4.30 \pm 0.19^{+0.14}_{-0.31}$
		60 – 70	64.8	$4.57 \pm 0.20^{+0.14}_{-0.17}$
		70 – 80	74.8	$4.46 \pm 0.24^{+0.15}_{-0.46}$
		80 – 90	84.9	$4.45 \pm 0.20^{+0.15}_{-0.25}$
		90 – 100	94.9	$4.72 \pm 0.21^{+0.15}_{-0.19}$
		100 – 110	104.9	$4.79 \pm 0.22^{+0.15}_{-0.36}$
		110 – 130	119.5	$4.71 \pm 0.16^{+0.14}_{-0.18}$
III	0.05	135 – 235	180.6	$5.08 \pm 0.14^{+0.25}_{-0.27}$
		205 – 305	250.7	$5.41 \pm 0.20^{+0.29}_{-0.40}$

Table 10: The slope parameter b derived from one-dimensional fits to the t dependence measured in bins of $W_{\gamma p}$. The values $\langle Q^2 \rangle$ and $\langle W_{\gamma p} \rangle$ are the bin centre values in the indicated ranges. The first error is statistical and the second systematic.

$\langle Q^2 \rangle$ [GeV ²]	r_{00}^{04}	r_{1-1}^{04}	R
0.05	$-0.030 \pm 0.016 \pm 0.027$	$0.020 \pm 0.016 \pm 0.042$	$-0.030^{+0.015+0.026}_{-0.015-0.025}$
3.2	$0.049 \pm 0.079 \pm 0.050$	$-0.129 \pm 0.070 \pm 0.039$	$0.052^{+0.096+0.059}_{-0.081-0.053}$
7.0	$0.19 \pm 0.14 \pm 0.06$	$-0.017 \pm 0.10 \pm 0.04$	$0.23^{+0.25+0.09}_{-0.18-0.08}$
22.4	$0.38 \pm 0.16 \pm 0.06$	$-0.04 \pm 0.12 \pm 0.04$	$0.62^{+0.59+0.17}_{-0.34-0.14}$

Table 11: The spin-density matrix elements, r_{00}^{04} and r_{1-1}^{04} , and the ratio of cross sections of longitudinally and transversely polarised photons R as a function of Q^2 in the range $|t| < 5 \text{ GeV}^2$ and $40 < W_{\gamma p} < 160 \text{ GeV}$. The values $\langle Q^2 \rangle$ indicate the bin centre values in the Q^2 range considered. The first error is statistical and the second systematic.

$\langle Q^2 \rangle$ [GeV ²]	r_{1-1}^1	$r_{00}^1 + 2r_{11}^1$	$r_{00}^5 + 2r_{11}^5$
3.2	$0.149 \pm 0.077 \pm 0.064$	$0.026 \pm 0.035 \pm 0.026$	$-0.035 \pm 0.072 \pm 0.055$
7.0	$0.43 \pm 0.11 \pm 0.06$	$0.062 \pm 0.054 \pm 0.028$	$-0.16 \pm 0.12 \pm 0.06$
22.4	$0.53 \pm 0.13 \pm 0.05$	$0.026 \pm 0.069 \pm 0.031$	$0.04 \pm 0.16 \pm 0.06$

Table 12: The spin-density matrix element r_{1-1}^1 and the combined elements $r_{00}^1 + 2r_{11}^1$ and $r_{00}^5 + 2r_{11}^5$ as a function of Q^2 in the range $|t| < 5 \text{ GeV}^2$ and $40 < W_{\gamma p} < 160 \text{ GeV}$. The values $\langle Q^2 \rangle$ indicate the bin centre value in the Q^2 range considered. The first error is statistical and the second systematic.

$\langle Q^2 \rangle [\text{GeV}^2]$	$\langle t \rangle [\text{GeV}^2]$	r_{00}^{04}	r_{1-1}^{04}
0.05	0.03	$0.003 \pm 0.039 \pm 0.028$	$-0.011 \pm 0.036 \pm 0.030$
	0.10	$0.011 \pm 0.043 \pm 0.029$	$-0.041 \pm 0.042 \pm 0.030$
	0.22	$0.026 \pm 0.036 \pm 0.028$	$0.104 \pm 0.035 \pm 0.029$
	0.43	$0.013 \pm 0.037 \pm 0.029$	$0.025 \pm 0.037 \pm 0.030$
	0.84	$0.047 \pm 0.041 \pm 0.029$	$0.064 \pm 0.047 \pm 0.034$
	1.8	$0.066 \pm 0.061 \pm 0.028$	$-0.010 \pm 0.060 \pm 0.030$
	3.5	$0.018 \pm 0.081 \pm 0.028$	$-0.074 \pm 0.082 \pm 0.032$
8.9	0.05	$0.32 \pm 0.15 \pm 0.06$	$-0.13 \pm 0.11 \pm 0.04$
	0.19	$0.22 \pm 0.13 \pm 0.06$	$-0.07 \pm 0.10 \pm 0.04$
	0.64	$0.05 \pm 0.10 \pm 0.05$	$-0.071 \pm 0.083 \pm 0.036$
	3.0	$0.23 \pm 0.19 \pm 0.06$	$0.06 \pm 0.13 \pm 0.03$

Table 13: The spin-density matrix elements, r_{00}^{04} and r_{1-1}^{04} , as a function of $|t|$ in the range $40 < W_{\gamma p} < 160 \text{ GeV}$ for photoproduction and electroproduction. $\langle Q^2 \rangle$ and $\langle |t| \rangle$ are the bin centre values. The first error is statistical and the second systematic.

$\langle t \rangle [\text{GeV}^2]$	r_{1-1}^1	$r_{00}^1 + 2r_{11}^1$	$r_{00}^5 + 2r_{11}^5$
0.05	$0.19 \pm 0.11 \pm 0.06$	$-0.16 \pm 0.12 \pm 0.06$	$0.031 \pm 0.055 \pm 0.029$
0.19	$0.62 \pm 0.11 \pm 0.06$	$0.04 \pm 0.10 \pm 0.06$	$0.004 \pm 0.048 \pm 0.026$
0.64	$0.361 \pm 0.097 \pm 0.061$	$-0.073 \pm 0.091 \pm 0.057$	$-0.039 \pm 0.043 \pm 0.027$
3.0	$0.07 \pm 0.15 \pm 0.06$	$-0.15 \pm 0.15 \pm 0.06$	$0.083 \pm 0.079 \pm 0.030$

Table 14: The spin-density matrix element r_{1-1}^1 and the combined elements $r_{00}^1 + 2r_{11}^1$ and $r_{00}^5 + 2r_{11}^5$ as a function of $|t|$ in the range $40 < W_{\gamma p} < 160 \text{ GeV}$ and $2 < Q^2 < 80 \text{ GeV}^2$. $\langle |t| \rangle$ indicates the bin centre value. The first error is statistical and the second systematic.